END
DATE
FILMED
5-82
DTIC

1.0

4.5
5.0
3.2
3.6
4.0

2.8
2.5
3.2
2.2
2.0

1.1

1.8

1.25   1.4   1.6

MICROCOPY RESOLUTION TEST CHART
NATIONAL BUREAU OF STANDARDS 1963 A

AFGL-TR-81-0352

FEASIBILITY ANALYSIS OF CLOUD FIELD PROPERTY
INFERENCE FROM BROADBAND RADIOMETRY

Research Institute of Colorado
Drake Creekside Two, Suite 200
2625 Redwing Road
Fort Collins, Colorado 80526

Stephen K. Cox

FINAL REPORT
25 February 1981 - 30 September 1981

September 1981

Approved for public release; distribution unlimited

AIR FORCE GEOPHYSICS LABORATORY
AIR FORCE SYSTEMS COMMAND
UNITED STATES AIR FORCE
HANSCOM AFB, MASSACHUSETTS 01731

DTIC
SELECT
APR 7 1982

A

AD A113133

DTIC FILE COPY

82 04 07 040

REPORT DOCUMENTATION PAGE		READ INSTRUCTIONS BEFORE COMPLETING FORM
1. REPORT NUMBER AFGL-TR-81-0352	2. GOVT ACCESSION NO. AD-A113 133	3. RECIPIENT'S CATALOG NUMBER
4. TITLE (and Subtitle) FEASIBILITY ANALYSIS OF CLOUD FIELD PROPERTY INFERENCE FROM BROADBAND RADIOMETRY		5. TYPE OF REPORT & PERIOD COVERED Final Report 25 February 1981-30 Sept 1981
		6. PERFORMING ORG. REPORT NUMBER
7. AUTHOR(s) Stephen K. Cox		8. CONTRACT OR GRANT NUMBER(s) F19628-81-K-0006
9. PERFORMING ORGANIZATION NAME AND ADDRESS Research Institute of Colorado Drake Creekside Two, Suite 200 2625 Redwing Road Fort Collins, Colorado 80526		10. PROGRAM ELEMENT, PROJECT, TASK AREA & WORK UNIT NUMBERS 63707F 268801AC
11. CONTROLLING OFFICE NAME AND ADDRESS Air Force Geophysics Laboratory Hanscom AFB, Massachusetts 01731 Monitor/Frederick Brousaides/LYS		12. REPORT DATE September 1981
		13. NUMBER OF PAGES 83
14. MONITORING AGENCY NAME & ADDRESS(if different from Controlling Office)		15. SECURITY CLASS. (of this report) Unclassified
		15a. DECLASSIFICATION DOWNGRADING SCHEDULE

16. DISTRIBUTION STATEMENT (of this Report)

Approved for public release; distribution unlimited

17. DISTRIBUTION STATEMENT (of the abstract entered in Block 20, if different from Report)

18. SUPPLEMENTARY NOTES

19. KEY WORDS (Continue on reverse side if necessary and identify by block number)

CLOUD COVER ESTIMATES
CLOUD DETECTORS
CLOUD FIELD PROPERTIES
BROADBAND RADIOMETRY

20. ABSTRACT (Continue on reverse side if necessary and identify by block number)

The goal of the study was to explore the capabilities of using passive radiometry to infer descriptive information about an overlying or underlying cloud field. Specific information includes cloud cover, cloud top height and cloud base height, as sensed by airborne broadband radiometers. The cloud information derived from implementation of passive radiometry will be used in tactical planning and as boundary conditions for short term meteorological prediction models.

DD FORM 1473
1 JAN 73

TABLE OF CONTENTS

iii

DTIO
COPY
INSPECTED
2
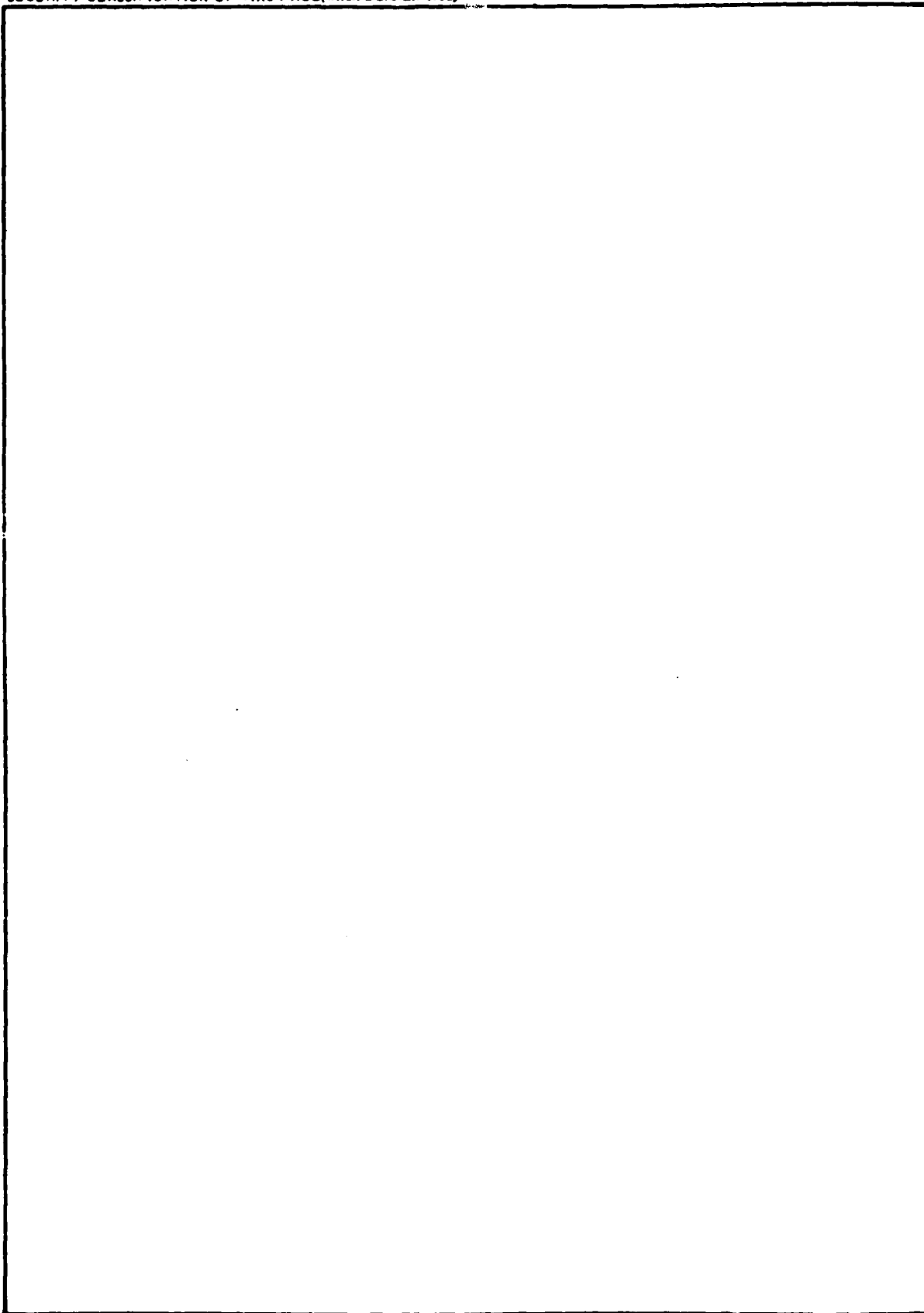
TABLE OF CONTENTS - Continued

LIST OF TABLES

v

LIST OF FIGURES

LIST OF FIGURES

vii

PREFACE

In this report we have documented the ability of passive radiometry to deduce meaningful information on cloud field properties. Passive radiometry is shown to be extremely flexible in that cloud field properties may be deduced from both direct and remote observations with these two modes being highly complementary. Relatively inexpensive, yet durable, detectors for wide band pass observations make the passive radiometry option even more appealing.

It would appear from this investigation that passive radiometry can give even more information than is actually required; therefore, the next step is to tailor a configuration to meet the specific requirements for the RPV application. Following this next step, prototype fabrication and in-field testing are the next obvious undertakings.

During the early stages of this research, it was determined not to pursue possible satellite alternatives to the cloudiness observation problem. However, it should be noted that some information on cloud cover and cloud top height can be determined from satellite infrared (11 micrometer) observations. The primary advantage of the satellite observation is its enhanced areal capability and the fact that it does not have to penetrate the air space of the observing region. However, satellite observations will not be able to determine cloud base height and will not offer as reliable information on cloud top height or cloud cover as the RPV mode. A recent paper on the ability of satellite data to depict cloud cover and cloud height is attached as Appendix C.

1

1. PROBLEM DEFINITION

The principal goal of this research is to explore the capabilities of using passive radiometry to infer descriptive information about an overlying or underlying cloud field.

Specific desired information includes cloud cover, cloud top height and cloud base height. Additional information on cloud element size, brightness and temperature contrast and angular variability of brightness may be sought as well.

The cloud information derived from implementation of passive radiometry will be utilized in ordnance selection, tactical planning and as boundary conditions for short-term meteorological prediction models.

2. SOLUTION OPTIONS

Wideband solar and wideband infrared radiometry will be evaluated for application to the problem posed above.

Three different deployment tactics for the wideband radiometers will be considered. They are i) aboard a RPV (remotely piloted vehicle), ii) implanted in the surface at a specific location, and iii) deployed in a dropsonde fashion where the radiometer(s) would gather data during descent.

3. SOLUTION CONSTRAINTS

Without some constraints an investigation such as this becomes boundless in terms of the possible avenues which might be explored. This study was conducted with the following principal constraints: i) the solution must be reasonably economical to allow for the strong possibility that the hardware would not be recovered. ii) The amount of data to be transmitted back to the decision point must not be excessive due to limited telemetry capability, and iii) any solution must have a strong physical, rather than empirical, relationship to cloudiness variables. With these constraints to bound our options, we have explored the application of passive radiometry to the problem of remotely determining cloudiness variables.

4

4.0 CLOUD FIELD INFORMATION RETRIEVAL TECHNIQUES

4.1 REMOTELY PILOTED VEHICLE MODE

One of the greatest advantages offered by the RPV deployment mode for wideband radiometers, is the flexibility offered by a mobile, "steerable" platform. Wideband radiometers can provide cloud field information of two types depending on the flight configurations being flown. The two types of information may be classified as direct and remote sensing information. The direct sensing configuration refers to a mode in which multiple flight levels are being flown and clouds are actually being penetrated. In this mode, cloud information is inferred from the vertical derivative of the wide band radiometer measurements. The second mode assumes that one deploys the RPV in more of a reconnaissance mode and does not actually penetrate the cloud layer while climbing from one altitude to another. The two modes are highly complementary as the direct mode yields accurate individual cloud height and base information while the remote mode, while still yielding height information, samples a broad region giving sufficient samples to assure the representativeness of a set of observations. The discussion below is divided into the two categories: direct and remote.

4.11 REMOTELY PILOTED VEHICLE-SOLAR OBSERVATIONS (.3 - 1 MICROMETERS)

4.111 DIRECT OBSERVATION MODE

The direct observation mode of cloud top and cloud base height assumes that the RPV actually penetrates the cloud base and/or the cloud top and in so doing collects data from below, within and on top of the cloud layer. The vertical divergence of the upward and downward solar irradiances through the layer will yield a strong indication of a change in the optical properties of the cloud layer and the clear air above

and below the layer. In the case of the cloud top, one would see a rapid transition from a highly anisotropic to a highly isotropic medium as one descends into the cloud layer. This phenomenon is shown in Section 6.1. Likewise, although to a lesser degree, the change from a more isotropic to more anisotropic distribution as one descends through the cloud base may be used to infer cloud base. In essence the solar device proposed for the remote information can be used as a simple nephelometer within the cloud layer itself.

4.1111 REMOTE OBSERVATION MODE

For the set of detectors lying in a vertical plane at angles relative to the local vertical directly beneath an aircraft, the widths of and time lags between the pulses observed by the different detectors contain information on the cloud properties. Figure 1 illustrates the relationships discussed below.

The width of the $N_{0°}$ pulse corresponds to the width of the cloud element. The times between the leading or falling edges of the pulses for different nadir angles are directly related to the cloud top height relative to the aircraft, i.e. $h = s(T_{1,0°} - T_{1,30°})/\tan 30°$ where s = speed of aircraft. The broadening of the pulses is principally related to the vertical extent of the cloud, i.e. $W_\theta = W_{0°} + z/\tan(\pi/2 - \theta)$. The sum of all pulse widths measured by a given detector yields a direct measure of "effective cloud cover" at the nadir angle of that detector, i.e. $q_\theta = \sum_{i=1,n} \frac{W_{\theta i}}{s \cdot \Delta t}$.

Likewise, any set of detectors oriented on a great circle arc passing through the center line of the RPV may be similarly related to the two horizontal dimensions of the cloud elements in the field. Figure 2 schematically illustrates a proposed solar

6
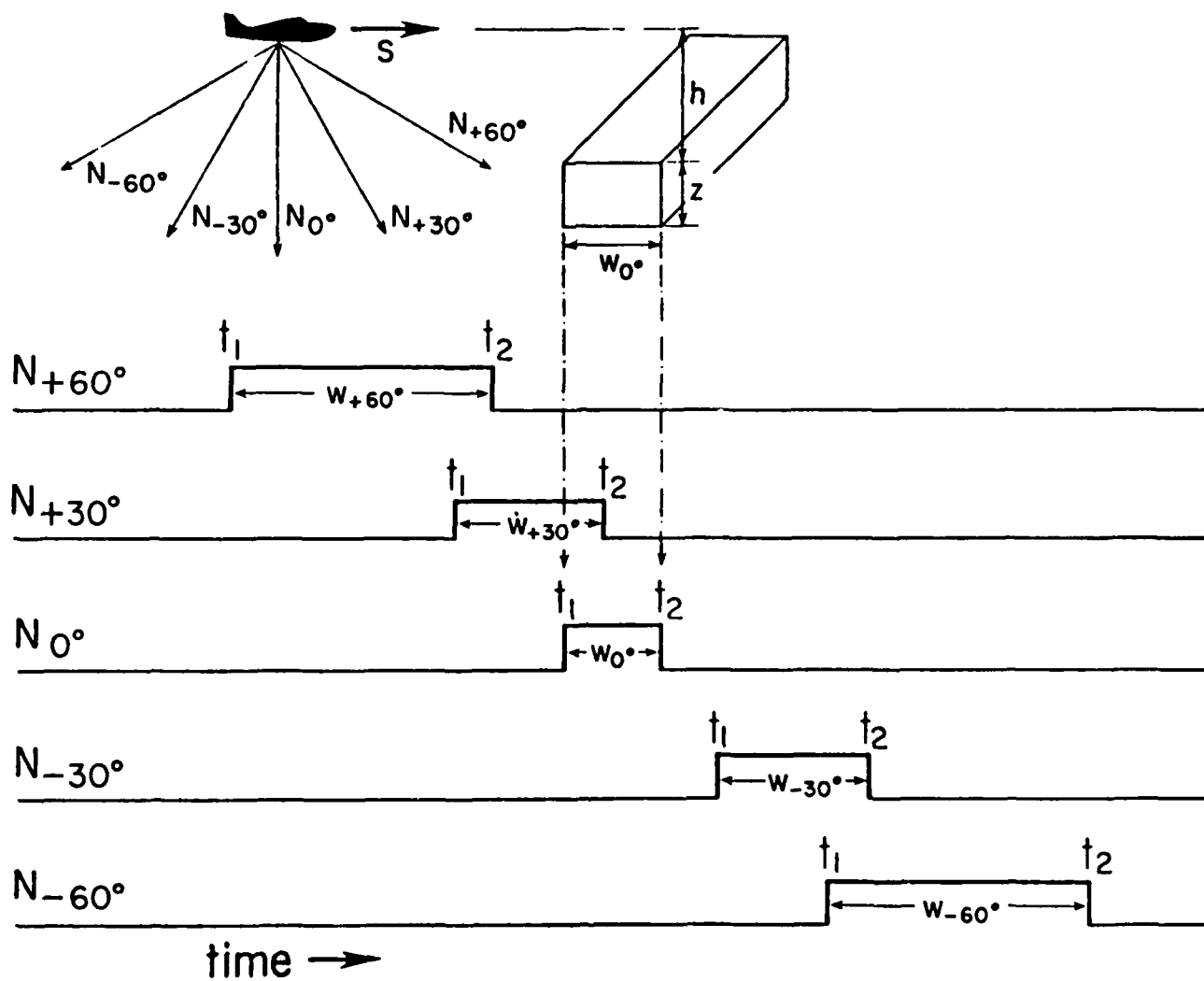
Figure 1. Schematic representation of solar remote observation mode.

7

Solar Prototype Configuration (Photodiode detectors)
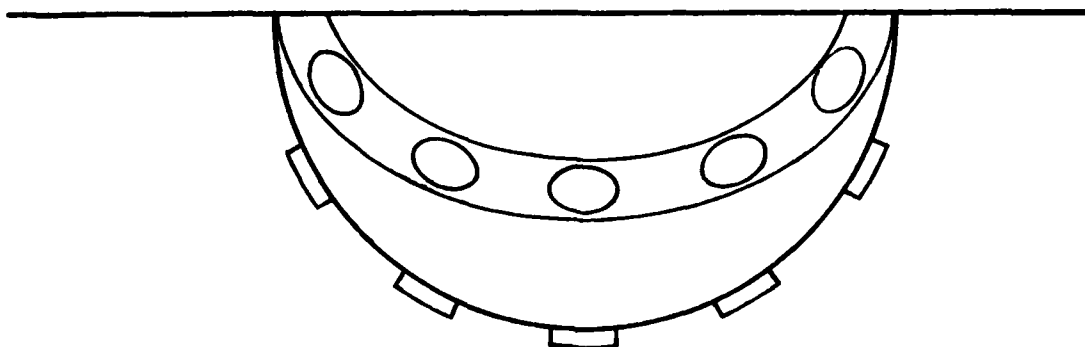
Fifteen photodiode detectors in 3-5 detector arrays. Each array
would lie on a great circle arc and detectors would be
displaced 30° of arc from one another. One array would
look into the nadir plane and the other two 45° away from
the nadir plane.

Figure 2. Schematic diagram of prototype solar detector array.

array configuration which would meet both direct and remote observation mode requirements.

4.12 REMOTELY PILOTED VEHICLE INFRARED OBSERVATIONS (7-14 MICROMETERS)

4.121 DIRECT OBSERVATION MODE

When the RPV is in a flight mode which allows actual penetration of cloud layers, the wide band infrared radiometers will allow direct inference of cloud top height and cloud base height. The principle of this deduction rests in the fact that there is a strong discontinuity in the infrared irradiance at cloud - clear air interfaces. The very strong radiative cooling associated with cloud top layers is widely recognized and readily observable because of its large magnitude. The cloud base also experiences a convergence of infrared irradiance which may be used as an indication of cloud base. This latter convergence is not as large as the divergence commonly associated with cloud top, however, it is certainly detectable.

A second direct observation mode would be a comparison of the two radiances N_{cldt} or N_{cldb} with N_{clds} (see sec. 4.122 & fig. 3). When the RPV is in the cloud layer, the three observations would be related by the following inequality $|N_{cldt} - N_{clds}| < \epsilon; |N_{cldb} - N_{clds}| < \epsilon$ where ϵ would be a relatively small value. As soon as the RPV approached either the cloud base or cloud top, the difference $|N_{cldt} - N_{clds}|$ or $|N_{cldb} - N_{clds}|$ would increase dramatically. This discontinuity would provide an excellent indication of cloud presence in the direct observation mode.

9

4.122 REMOTE OBSERVATION MODE

In order to deduce cloud field properties from infrared broad-band radiometry without an inordinate number of somewhat questionable assumptions, we have devised a multiple detector scheme which uses a wide field of view detector to yield areal sampling and several narrow field of view detectors to measure specific high resolution features essential in the analysis. Figure 3 schematically represents the proposed sensor configuration and associates each sensor with terms in the reduction equation. The reduction equation derivation is given in appendix D. In figure 3, "L" represents the component of the irradiance measured by the wide field of view detector (in this case 90 deg.). N_{clr} and N_{cldt} represent the observed clear sky upwelling radiance and the upwelling radiance from cloud top, respectively; in this case both would be measured from a nadir viewing narrow field of view detector. N_{clds} represents the side looking radiance received from cloud sides; this parameter would be deduced from a narrow field of view detector looking slightly below the horizon. Each of the above mentioned parameters are measured directly. q in the equation is the fractional cloud amount the beta is the cloud aspect ratio (the ratio of the mean lateral cloud dimension to the cloud height). Thus we have reduced the solution for the fractional cloud amount to four measurements and one assumed cloud aspect ratio value.

Cloud top height would be determined from relating the N_{cldt} value to an equivalent temperature on a temperature-height scale. One might note that with an estimate of surface temperature from N_{clr} and the air temperature at aircraft altitude, a mean lapse rate for the layer and thus the pressure-temperature-height relationship is also established to the first order. The above comments assume that the

IR Prototype Configuration (Pyroelectric detectors)

$$q = \frac{L - \pi\,N_{CLR}\left[1 - \cos^2 45°\right]}{\pi\left(1 - \cos^2 45°\right)\cdot\left(N_{CLDT} - N_{CLR}\right) + \frac{1}{\beta}\left(\pi - 1\right)\cdot\left(N_{CLDS} - 1\right)}$$
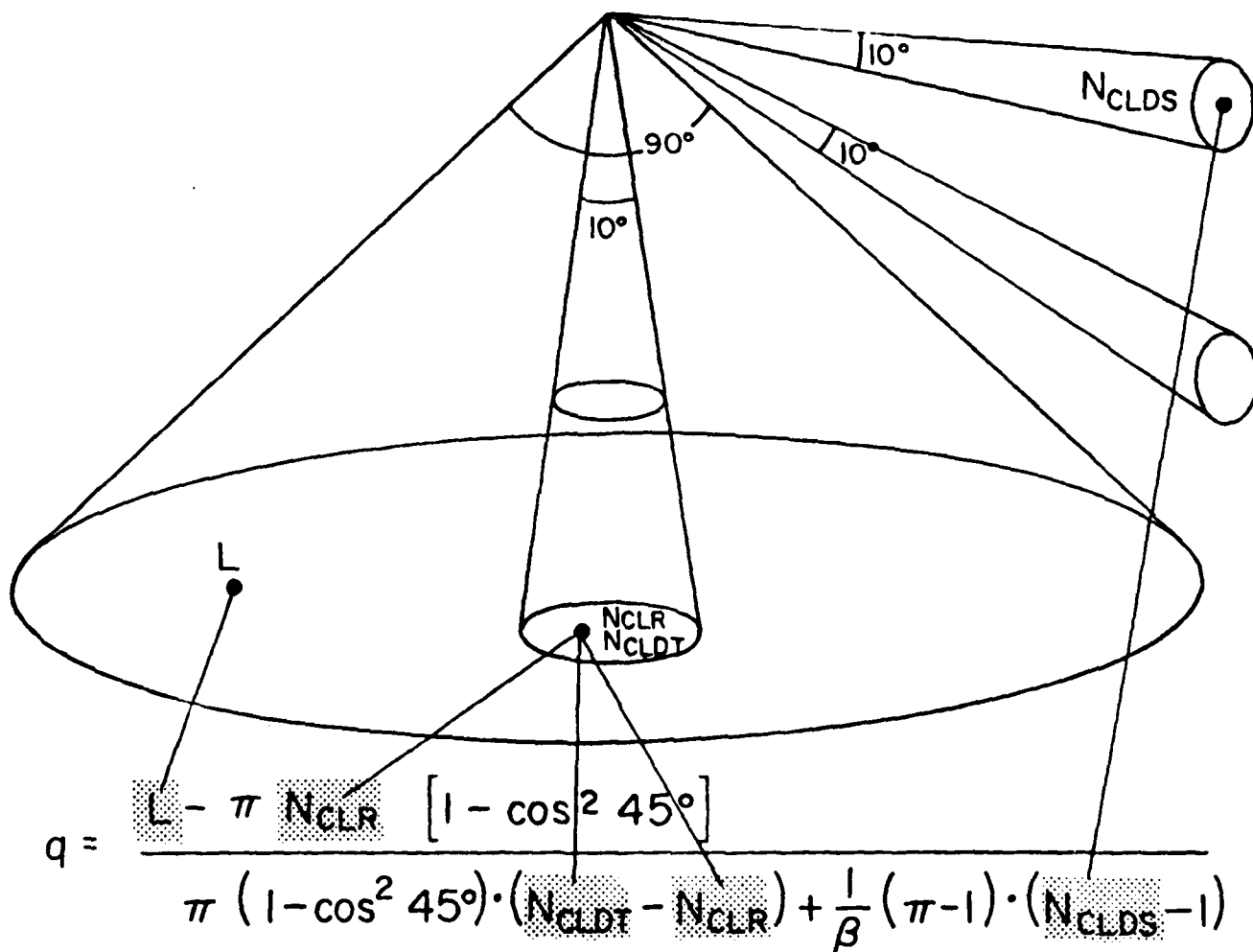
Figure 3. Schematic diagram of prototype infrared detector array.

11

observations would all be collected from one level; if multiple levels
are sampled, detailed structure of the lapse rate could be readily
included in the cloud top height analysis. Similarly, if a cloud top or
base is penetrated on ascent or descent, a strong direct indication of
cloud presence will be obvious from the nadir and zenith detectors.

The analysis procedure described above can be applied to the down-
ward looking hemisphere where fractional cloud cover and cloud top
height are the primary desired information; the entire scheme may be
flipped over to view the upward hemisphere where the desired information
becomes fractional overhead sky cover and cloud base height. In this
application, N_{clr} is the downwelling clear sky radiance and N_{cldt} in
the equation really becomes N_{cldb}, the downwelling radiance from the
cloud base. The analysis procedure for the cloud base height proceeds
in a manner analogous to that for the cloud top height.

In addition to the cloud field properties inferred from the
radiation data, there is a vast amount of potentially very useful
information on the target-scene radiative brightness and contrast
content. Since the detector to be employed covers the 8 to 14 micron
spectral bandpass, its output will be closely related to what a narrower
spectral bandpass instrument would measure in the 10 to 11 micron bandpass.
This is why an additional narrow field of view detector is shown in figure
3. The brightness and contrast measured by such a detector would yield
additional scene information, not necessarily cloud data, but never-
the-less potentially valuable decision-making information.

12

4.20 DROPSONDE MODE

4.21 INFRARED - OBSERVATIONS

Cox (1971) proposed that an effective way to discern cloud top
and base heights from broadband infrared measurements was to compare
the infrared divergence observed in a given layer with that calculated
assuming the layer to be saturated with water vapor. An extension
of this work has shown that upward and downward irradiances should prob-
ably be analyzed separately using the divergence of the downward irradiance
to discern the cloud top and the upward irradiance to discern the cloud
base. The two can be used together to resolve some ambiguity resulting
from broken cloud fields advecting below the radiometer.

Kuhn (1963) clearly demonstrated that a broadband parameter
derivable from broadband infrared measurements could be used to infer
cloud layers. The parameter, called the equivalent infrared radiation (F_E)
is the sum of the upward and downward infrared irradiances divided by
two. Ph,:ically this parameter represents the radiative equilibrium
temperature that a flat disc would attain if it were suspended in a
vacuum with the individual irradiance streams incident upon it. Examples
of this application are shown in section 6.3.

4.22 SOLAR - OBSERVATIONS

Any measurement made in the solar broadband dropsonde mode to infer
cloud top height will most likely be based upon solar extinction.
Basically an upward looking instrument will be receiving a direct solar
component when the instrument is above the cloud; upon entering a cloud
top the irradiance will likely momentarily increase and then decrease
sharply. This dramatic gradient provides a reliable indication of cloud
top unless there is a relatively opaque cloud layer at higher altitudes.

13

5. DERIVABLE INFORMATION FROM PASSIVE RADIOMETRY

Table 1 below lists the information on cloudiness derivable from
broadband radiometry for RPV and DS modes. The techniques employed in
each case were outlined in section 4.

Two basic types of information are referred to in Table 1. They
are cloud field properties and radiative brightness information.
Cloud field property inferences from passive radiometry rely, for
the most part, on discriminating cloud radiative signatures against
a background radiation scene. For instance, at visible wavele gths
clouds are generally brighter than underlying surfaces; for infrared
wavelength clouds are generally colder and thus contrast with a warmer
surface background. It is this contrast in both wavelength regions which
allows us to infer cloud field properties. This same contrast between
target and background is used for targeting weaponry. Therefore,
passive radiometry yields not only potentially useful cloud field information,
but, also scene brightness variation data in two spectral regions commonly
used to target weaponry. Although the spectral bandpass to be used will
be much broader, the variability between it and its narrower bandpass
counterpart will be highly correlated.

TABLE 1.   INFORMATION AVAILABLE FROM DIFFERENT PASSIVE RADIOMETRY DEPLOYMENT MODES

Deployment Mode	Cloud Field Information		Other Information
	Single level	Multi level	
Aircraft			
IR uplooking	Base ht.; Q_{ovcst}	Base ht.; Top ht.; Q_{undcst}; Q_{ovcst}	Scene IR brightness variability
IR downlooking	Top ht.; Q_{undcst}	Base ht.; Top ht.; Q_{undcst}; Q_{ovcst}	Scene IR brightness variability; Equivalent BB sfc temperature
SW uplooking	Q_{ovcst}; STX	Q_{ovcst}; STX; top ht.[1]	Scene SW brightness variability
SW downlooking	Q_{undcst}; Top ht.; Base ht.; STX	Q_{undcst}; Top ht.; Base ht.; STX	Scene SW brightness variability
Dropsonde			
IR	Top ht.[1]; Base ht.[1]		Equivalent BB sfc temperature
SW	Top ht.[1]		

[1] Requires cloud penetration

Symbol Definitions

Base ht. = cloud base height
Top ht. = cloud top height
IR = infrared
SW = solar
BB sfc = black body surface

Q_{ovcst} = overcast fractional cloud cover
Q_{undcst} = undercast fractional cloud cover
STX = statistical description of cloud and cloud free dimensions

15

6.0 EVIDENCE OF FEASIBILITY OF USING PASSIVE RADIOMETRY TO INFER CLOUD FIELD CHARACTERISTICS

There have been a number of investigations reported, in both the formal and informal literature, which show the feasibility of determining cloud field properties from passive radiometric measurements. Although most of these applications have been aimed at energy budget applications in the atmospheric sciences, they clearly establish the potential for using passive radiometry to meet the objectives of this investigation. In this section a number of these investigations will be introduced and the salient points discussed.

6.1 REMOTELY PILOTED VEHICLE - SOLAR (.3 - 1 MICROMETER)

6.11 DIRECT OBSERVATION MODE

Figures 4-6 illustrate the change in both the magnitude and the angular distribution of solar radiation in the upper hemisphere at cloud top and at cloud base. These data were collected on a cloud penetration flight path using a multi-detector photodiode instrument. The change in the degree of isotropy as one penetrates the cloud top from above is illustrated obviously from a comparison of Figures 4 and 5. The same detector configuration would be used in the direct observation mode and the remote observation mode discussed in the next section.

6.12 REMOTE OBSERVATION MODE

The methodology proposed to infer cloud field properties from a multi-directional solar array was outlined in section 4.1.

The application of the methodology using a multi-directional solar array to infer cloud field properties was tested using a data set which was collected for an unrelated purpose. As a result,

16
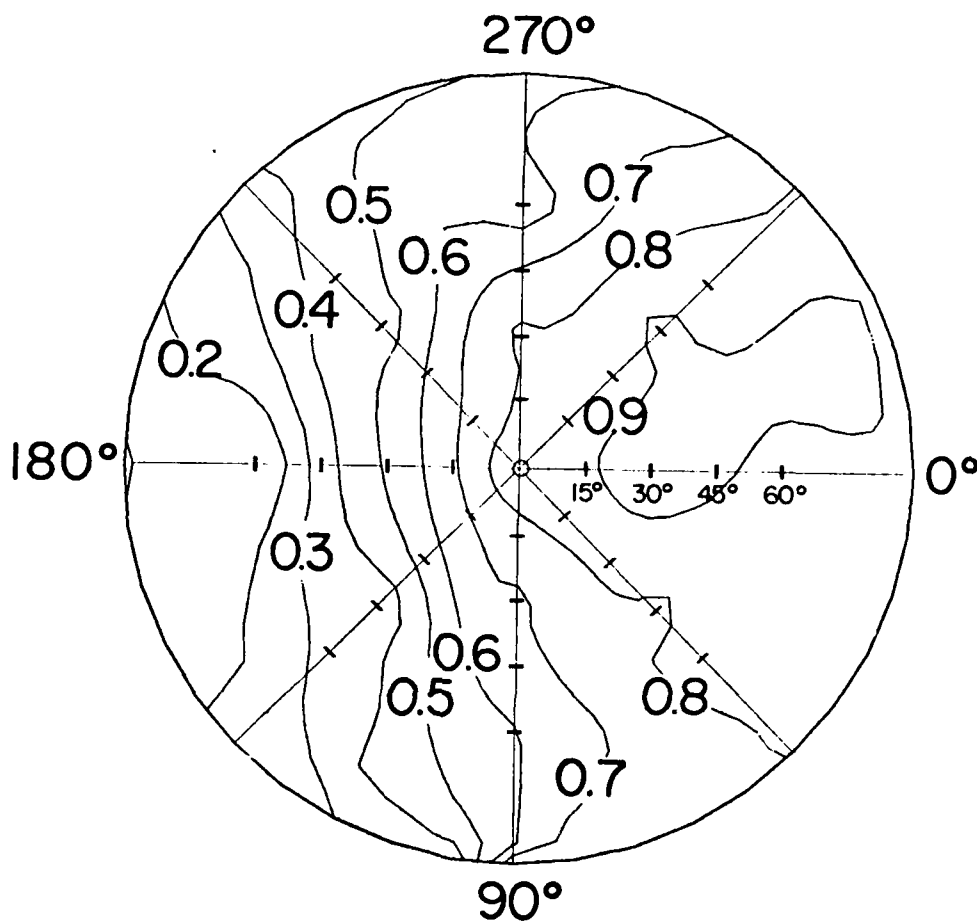
IRRADIANCE PATTERN OF CLEAR SKY

MIN = .03

MAX = .98

Small numbers on radial axes are zenith angles.
Large numbers on circumference are azimuth angles.

Figure 4.   Irradiance pattern of clear sky (relative values).

17
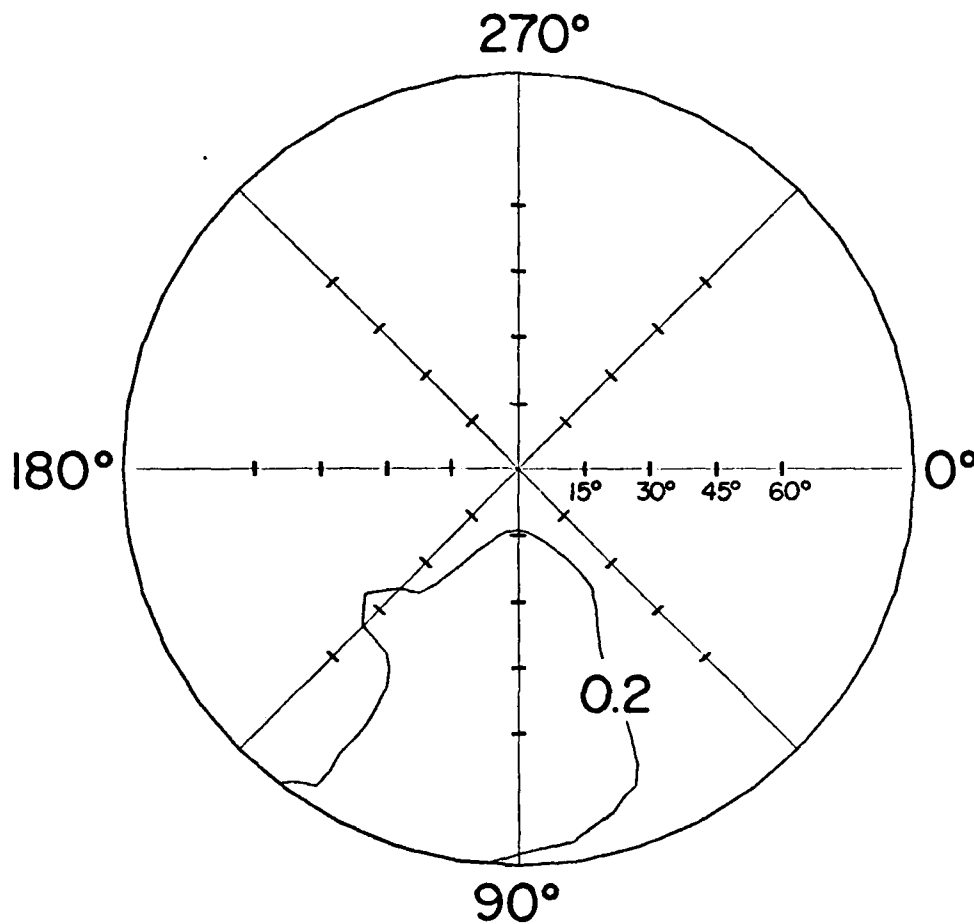
IRRADIANCE PATTERN BELOW SEVERAL STRATUS CLOUD
LAYERS

MIN = .15

MAX = .27

Small numbers on radial axes are zenith angles.

Large numbers on circumference are azimuth angles.

Figure 5. Irradiance pattern below several stratus cloud layers
(relative values).

18
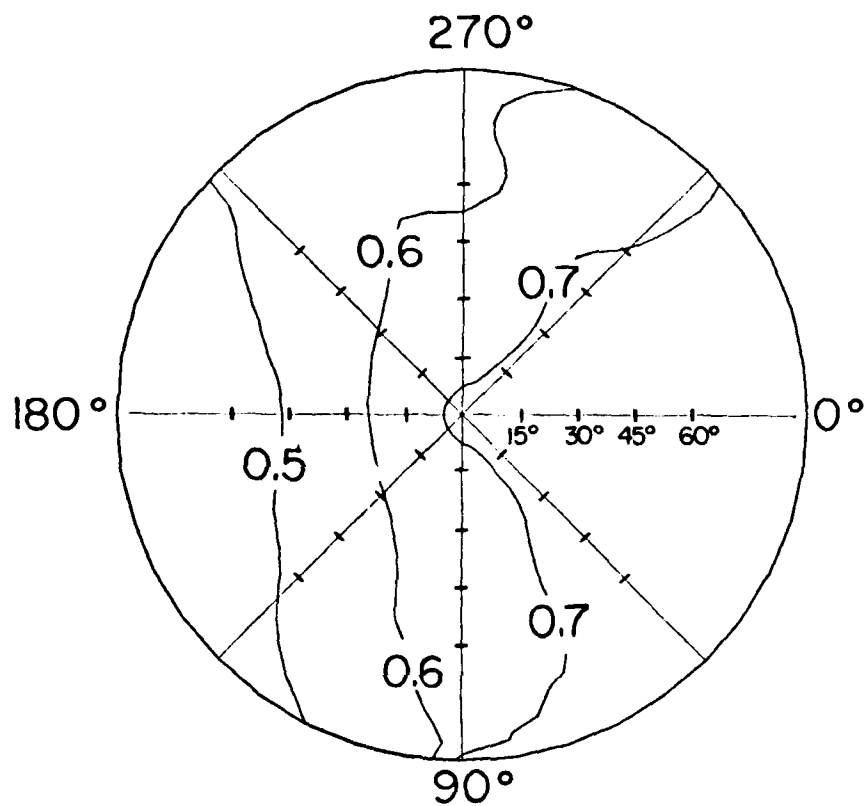
IRRADIANCE PATTERN AT THE BASE OF A CIRROSTRATUS
CLOUD

MIN = .36
MAX = .71

Small numbers on radial axes are zenith angles.
Large numbers on circumference are azimuth angles.

Figure 6. Irradiance pattern at the base of a cirrostratus cloud.

19

neither the detector resolution, the detector array, nor the flight plan was optimized for the cloud field data analysis.

Four segments of data representing different cloud field types were analyzed from a data set collected during the Spring of 1978 as part of Summer Monex field experiment. Figures 7-10 show six photograph sequences of each of the four cases considered in the following analysis.

Table 2 shows the results of determining the cloud top height obtained by applying a lag covariance technique to determine the cloud top height. In two of the cases independent estimates of the cloud height were available. It must be pointed out that the instrument resolution theoretically limited the cloud top height accuracy to 1000 feet. The range of values represented in the instrument derived cloud height column represents the total range of values obtained by performing the lag covariance analysis to each pair of the five detector set available. This analysis clearly shows that, even without optimizing detector field of view and orientation, cloud height information can clearly be inferred using this technique.

Table 3 shows the types of individual statistics on cloud dimensions and clear space dimensions observed during the same cases analyzed in table 2. Again, clearly, the non optimized solar detector array can discriminate important, decision-making information on cloud field characteristics for a variety of cloud regimes. The zero standard deviation values merely indicate that only one cloud/ space was present during the sample.

One final note on table 2, is the ability of the technique to discern cloud height even in the nearly overcast alto stratus case; this
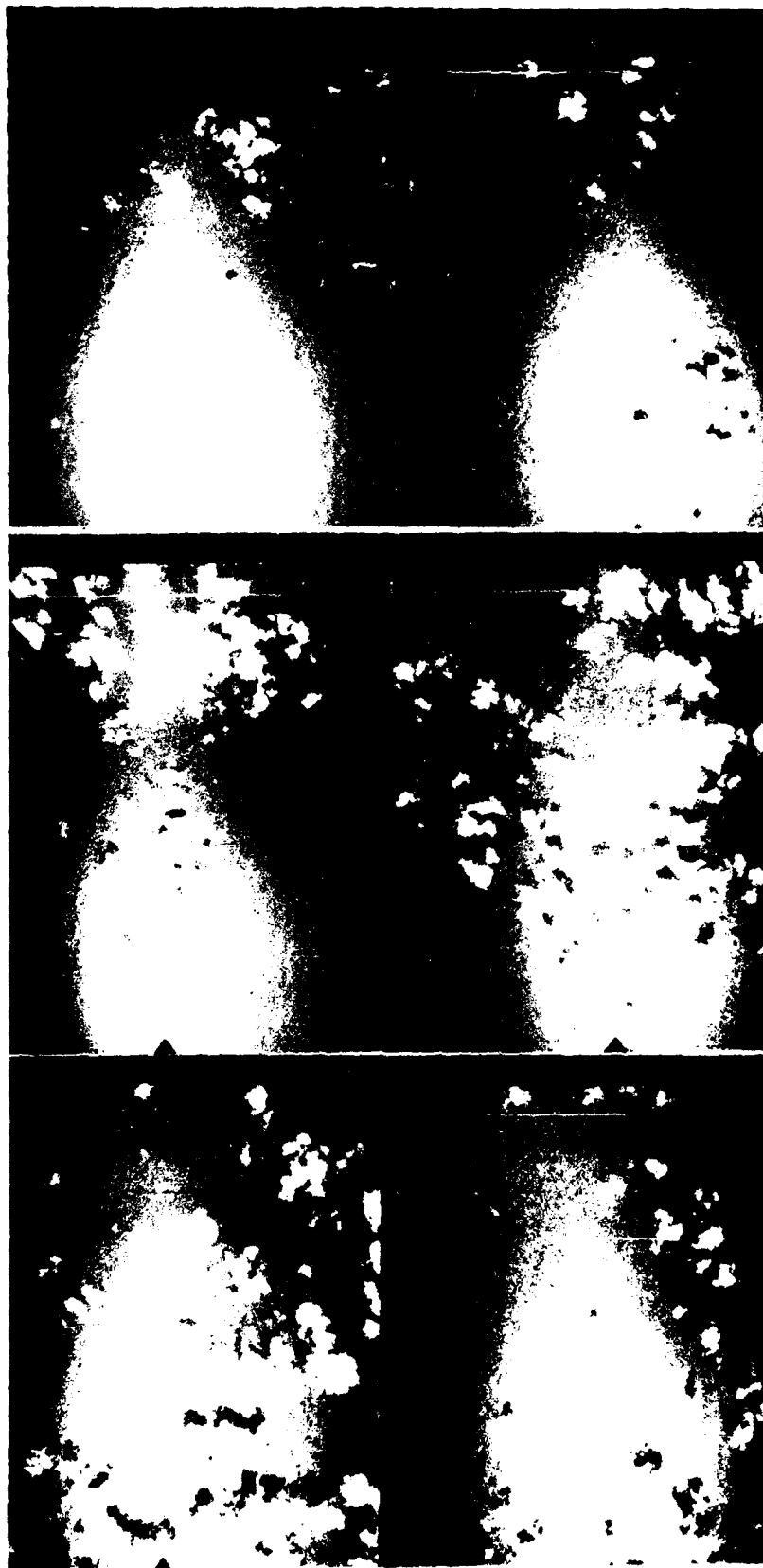
FIGURE 7
Six Photographic Sequence of
FAIR WEATHER CUMULUS
Case Referred to in Table 2

FIGURE 8
Six Photograph Sequence of
TOWERING CUMULUS
Case Referred to in Table 2

FIGURE 9
Six Photograph Sequence of
ALTOCUMULUS
Case Referred to in Table 2
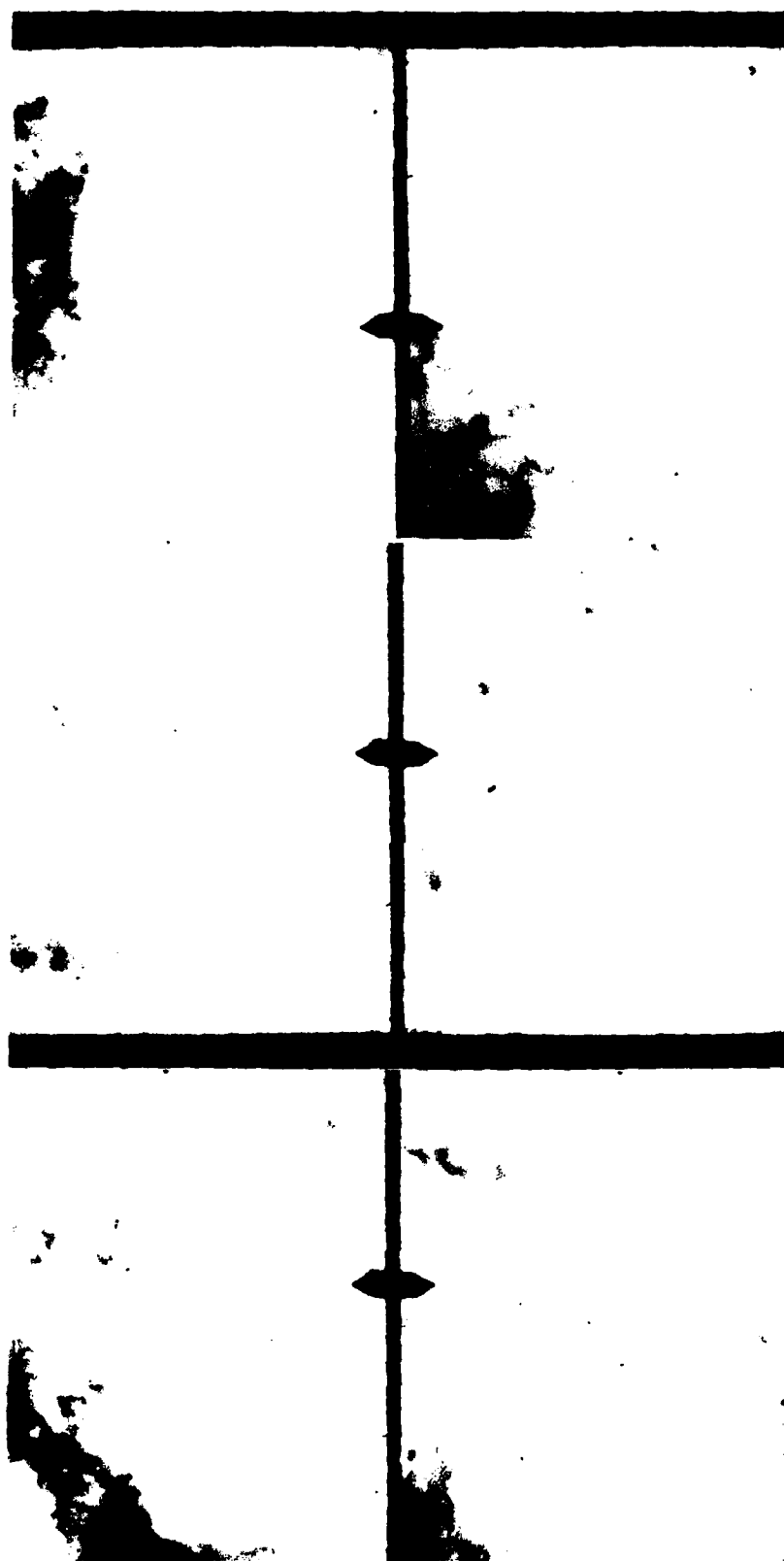
FIGURE 10
Six Photograph Sequence of
ALTOSTRATUS
Case Referred to in Table 2

CLOUD TYPE	AIRCRAFT ALTITUDE (FT)	ESTIMATED CLOUD HEIGHT (FT)	INSTRUMENT DERIVED CLOUD HEIGHT (FT)
FAIR WEATHER CUMULUS	33,500	3,000 TOPS	3,500 ± 800
TOWERING CUMULUS	37,200	NA	10,300 ± 2,000
ALTOCUMULUS	35,200	20,000 TOPS 18,000 BASES	18,500 ± 400
ALTOSTRATUS	37,200	NA	12,800 ± 1,100

CLOUD HEIGHT DERIVED FROM LAG COVARIANCE ANALYSIS.
EACH INSTRUMENT DERIVED HEIGHT IS THE AVERAGE OF 10 LAG COVARIANCE
ESTIMATES AMONG 5, 10° FIELD OF VIEW SENSORS.

TABLE 2. CLOUD HEIGHTS DERIVED FROM LAG COVARIANCE ANALYSIS.

CLOUD TYPE	SENSOR POSITION +(FORWARD) -(BACKWARD)	CLOUD ELEMENT DIMENSION IN KM MEAN STD. DEV.	CLOUD SPACING IN KM MEAN STD. DEV.
	+60	26.4, 0.0	106.0, 21.2
FAIR WEATHER	+30	4.7, 6.4	56.0, 41.6
CUMULUS	0	5.4, 5.9	76.0, 36.4
	-30	1.3, 1.6	7.6, 21.2
	-60	12.2, 0	114.0, 23.0
	+60	12.1, 19.3	30.0, 50.3
TOWERING	+30	15.0, 10.9	32.3, 50.0
CUMULUS	0	7.7, 7.1	27.4, 34.4
	-30	6.3, 5.6	23.1, 28.5
	-60	46.3, 31.3	88.3, 110.5
	+60	27.6, 35.8	31.6, 39.8
	+30	4.0, 2.0	12.8, 33.1
ALTOCUMULUS	0	2.9, 1.4	11.8, 31.8
	-30	4.5, 3.2	10.3, 32.8
	-60	16.9, 3.2	30.8, 60.4
	+60	95.0, 127.0	24.1, 5.5
	+30	65.0, 106.0	14.7, 10.6
ALTOSTRATUS	0	240.0, 0.0	0.0, 0.0
	-30	240.0, 0.0	0.0, 0.0
	-60	105.0, 146.0	22.6, 0.0

TABLE 3. Means and standard deviations of the intervals above and below
cloud threshold in kilometers for various cloud types and sensor
orientations.

is apparently due to brightness variations on the top of the cloud deck.

6.20 REMOTELY PILOTED VEHICLE - INFRARED (7 to 14 MICRONS)

6.21 DIRECT OBSERVATION MODE

Figures 11 and 12 from Paltridge and Platt (1974) and Griffith and Cox, respectively, illustrate the broadband infrared irradiances as a function of height through a water cloud and ice cloud. The discontinuity in the net irradiance at the cloud top is clearly indicated. (Note: the net irradiance is the difference between the upward and downward irradiances while the cooling rate is proportional to the vertical derivative of the net irradiance). The effect of the cloud base is a little more subtle, but can generally be detected as actual convergence or, at least, as a minimum of divergence in the net irradiance profile.

6.22 REMOTE OBSERVATION MODE

No appropriate data were available to evaluate the infrared strategy outlined in Appendix D; therefore, no analysis based upon real data was made.

6.30 DROPSONDE METHODOLOGY

The only data readily available to the contractor to test the dropsonde mode was infrared data obtained from an up-sonde with an economical radiometer [Suomi and Kuhn (1958)]. These data were collected by the principal investigator in the mid 1960's as part of an ongoing study of the radiation budget of the atmosphere. Figures 13 and 14 reproduced from Kuhn (1963) present representative samples of the ability of such a device to discern cloud top height and to a slightly less reliability, cloud base height.
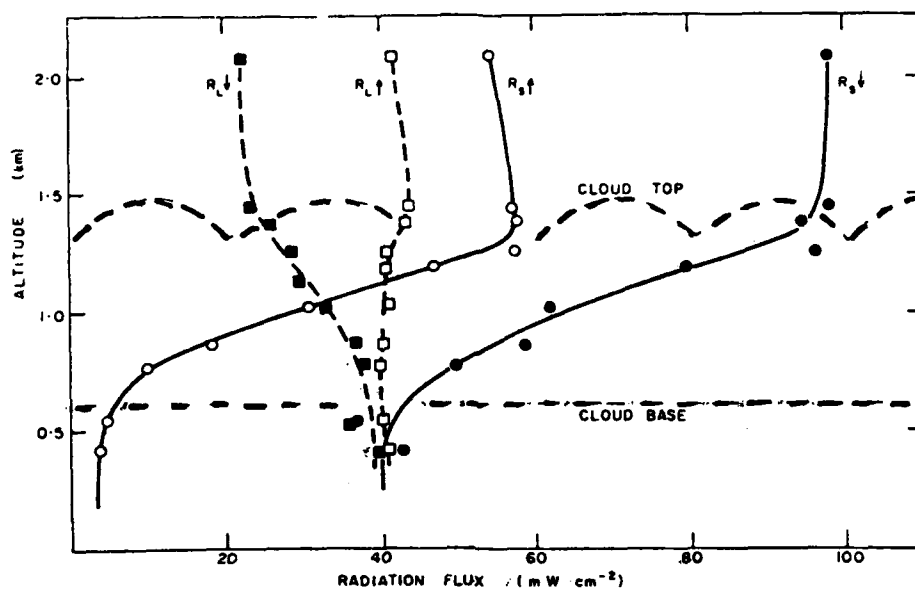
Fig.11 Radiation profiles through cloud on December 5, 1971. Note turreted cloud top   (Paltridge, 1974)

ALTITUDE (km)
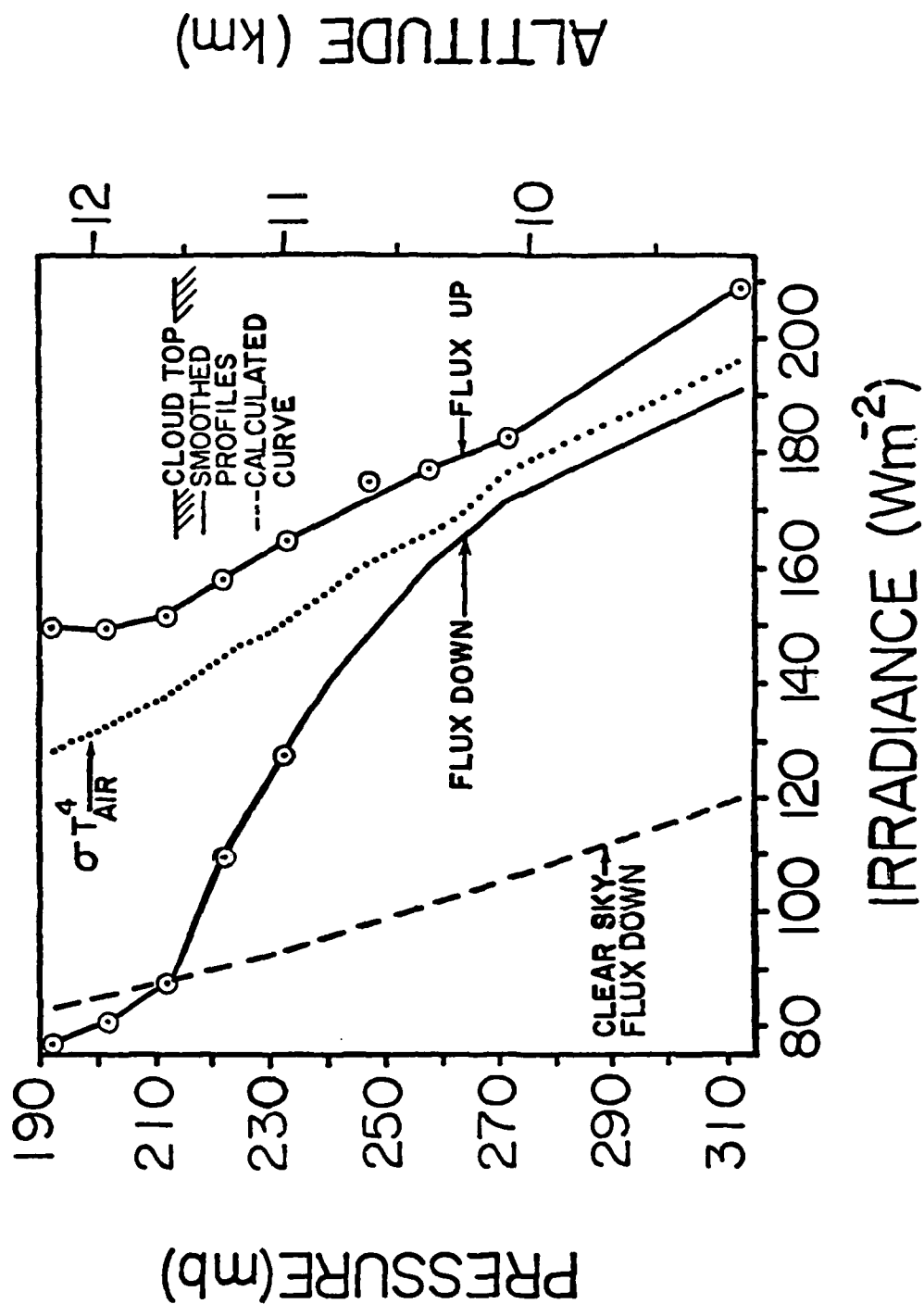
Figure 12. Infrared irradiance profiles through a cirrostratus layer.
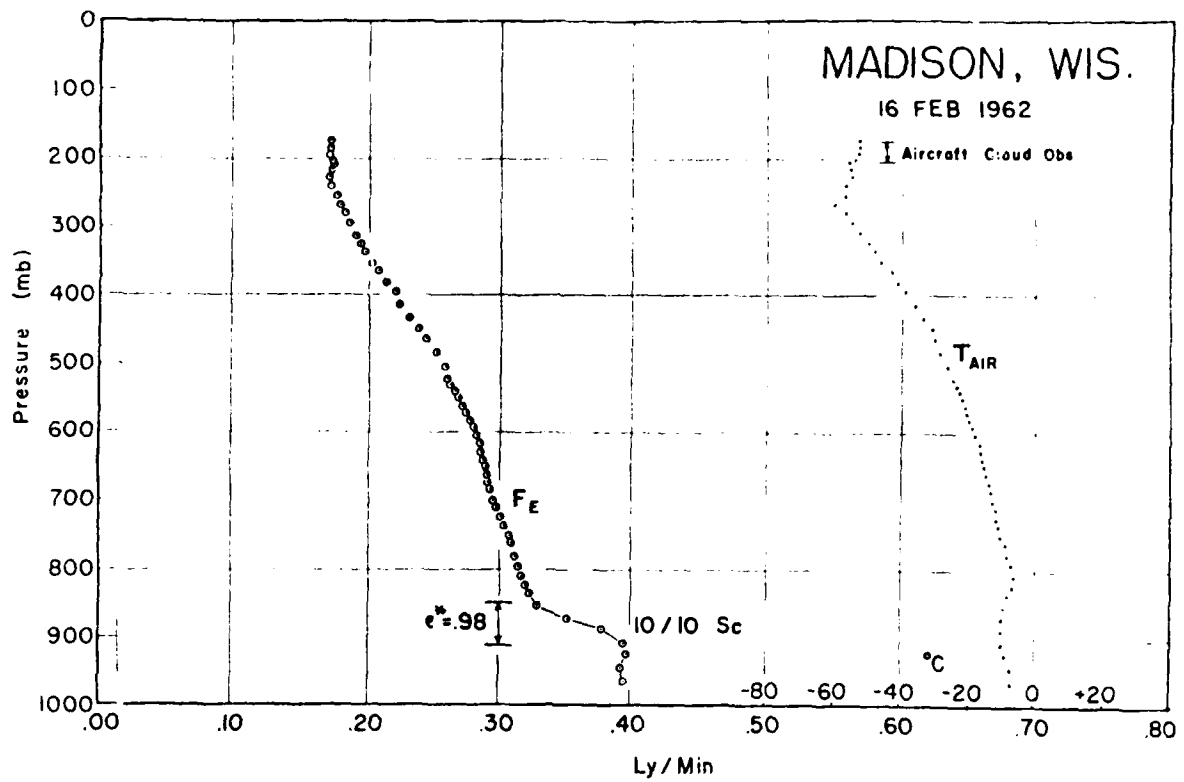
—Equivalent radiation, F_E, air temperature, T_{AIR}, and mixing ratio, Q, Madison, Wis., February 16, 1962.
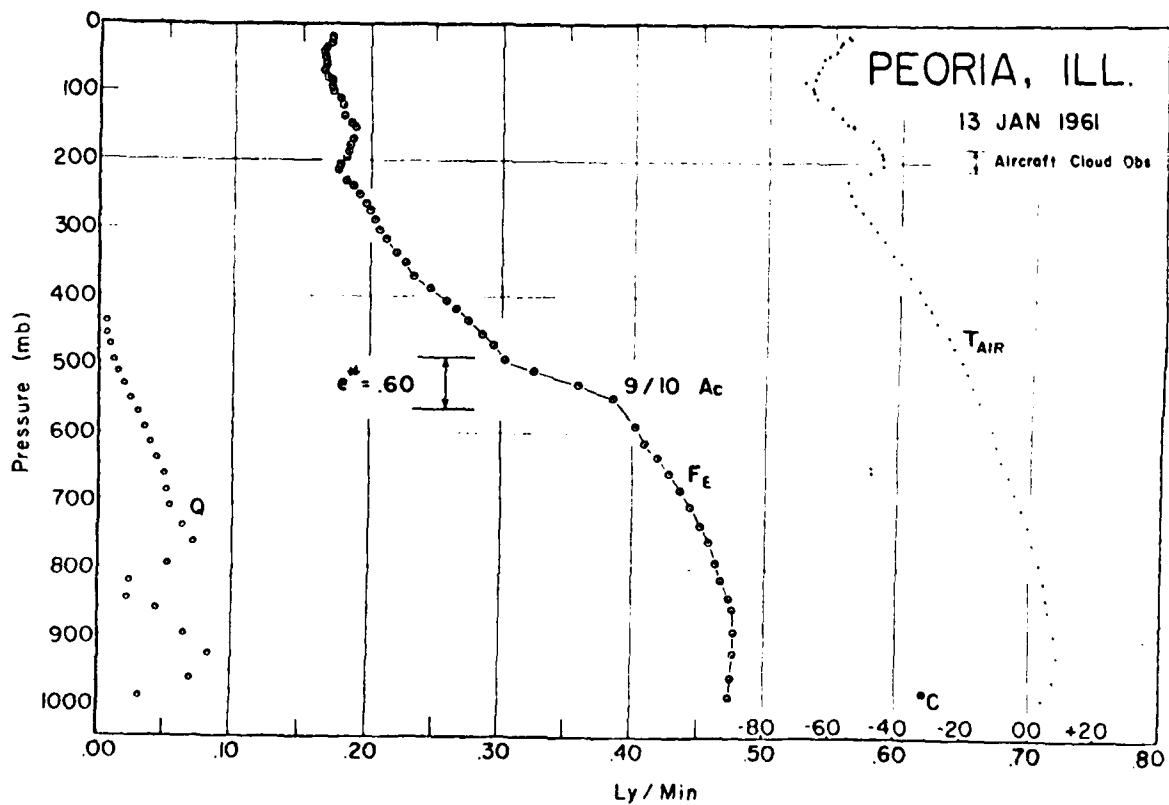
Figure 13.—Equivalent radiation, F_E, air temperature, T_{AIR}, and mixing ratio, Q, Peoria, Ill., January 13, 1961.
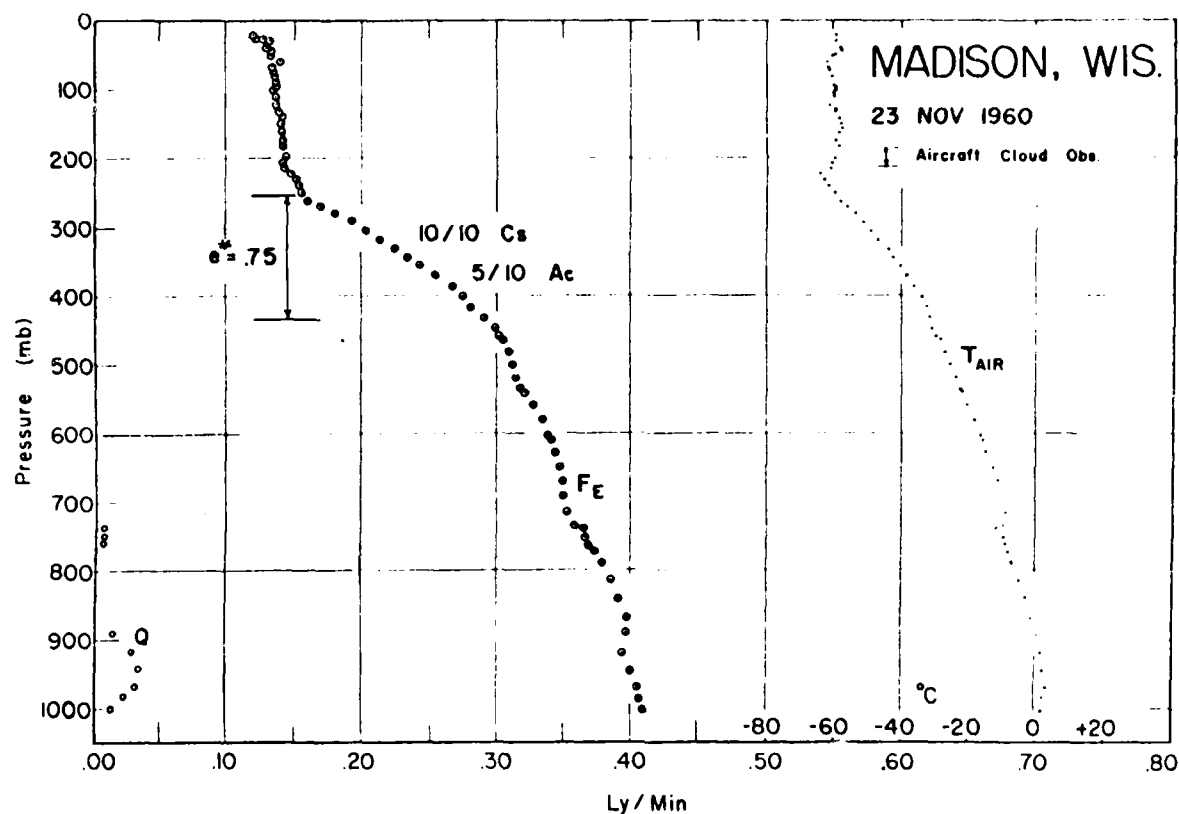
−Equivalent radiation, F_E, air temperature T_{AIR}, and mixing ratio, Q, Madison, Wis., November 23, 1960.
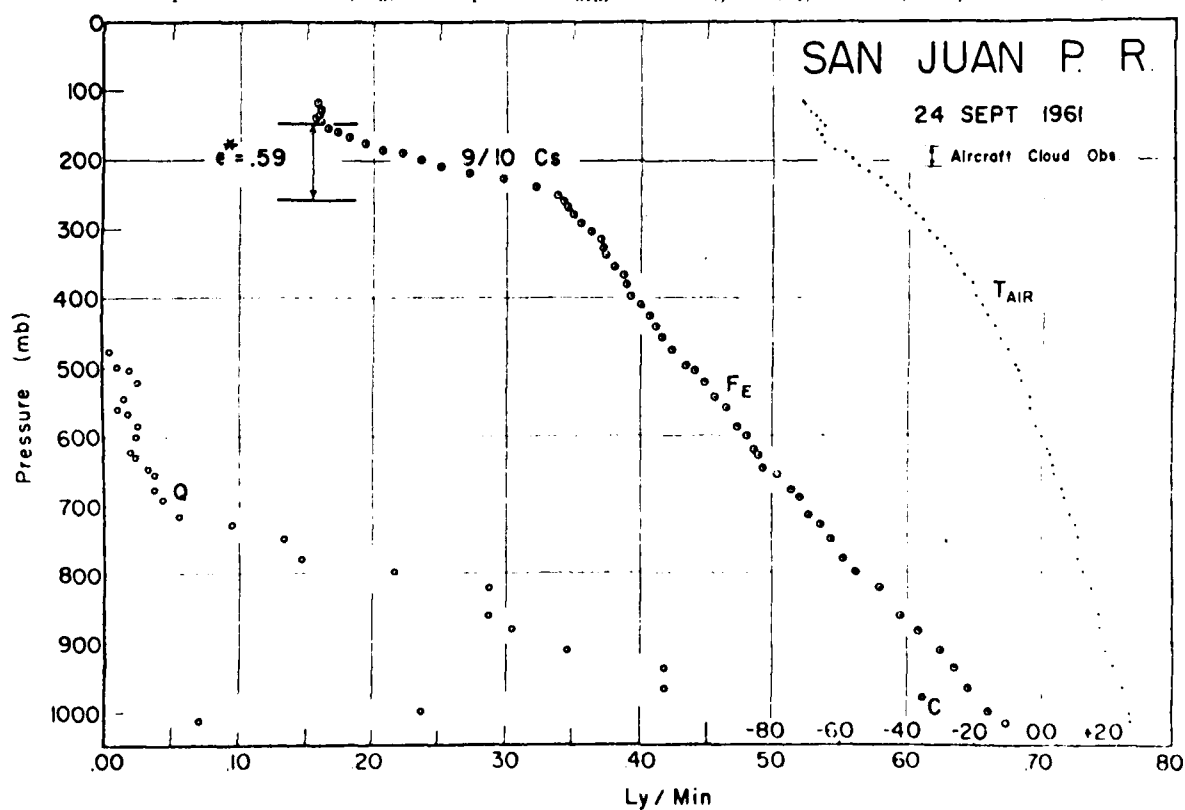
FIGURE 14.—Equivalent radiation, F_I, air temperature, T_{UR}, and mixing ratio, Q, San Juan, P.R., September 24, 1961.

31.

TABLE 4: A QUANTITATIVE RATING OF PASSIVE RADIOMETRY DEPLOYMENT MODES

| | SOLAR SENSOR | | | | INFRARED SENSOR | | |
| | REMOTELY PILOTED VEHICLE | | DROPSONDE | GROUND IMPLANT | REMOTELY PILOTED VEHICLE | | DROPSONDE |
Row	A Single Altitude	B Multi Altitude	C	D	E Single Altitude	F Multi Altitude	G
1 Sky Cover	8	10	1 to 8*	5 to 8*	8	10	2 to 8*
2 Cloud Top Height	8	10	7	0	9	10	8
3 Cloud Base Height	6	9	3	5	0	8	4
4 Horizontal Dimension 1	9	9	0	5	2	2	0
5 Horizontal Dimension 2	5	5	0	0	0	0	0
6 Areal Sample	10	10	1 to 10*	4 to 6*	10	10	1 to 10*
7 Cloud Statistics	10	10	0	1	6	6	0
8 Sample Time	10	7	5	1 to 3*	10	8	5
9 Flexibility	8	9	5 to 8*	0	8	9	5 to 8*
10 Cost Effectiveness	10	9	5	4 to 2*	10	9	5
11 Limitations	-4	-4	-5	-10 to -6	10	10	-3 to 0
12 Rating	80	84	22 to 36*	15 to 24	73	82	27 to 45*

Table 4. Figures of merit for various passive radiometer deployment configurations to infer cloud field properties.

*This value would vary according to the number of instruments committed to a given area. The right hand value would apply if 1 unit/Km^2 were committed. The values to the left apply for densities about 1 unit/10 Km^2.

7. QUANTITATIVE ASSESSMENT OF INDIVIDUAL DEPLOYMENT MODES

Table 4 lists a quantitative evaluation of each of the three deployment modes for both the solar and infrared broadband radiometer applications. Each mode is evaluated independently and no attempt is made in this section to consider multiple simultaneous deployment modes. Appendix A elaborates on the rationale for the numerical rating given in each table entry.

The most obvious conclusions that may be drawn from table 4 are that the RPV mode of deployment for passive radiometers is far superior to either the dropsonde or ground implant mode of deployment. The ground implant mode is so inferior for the purpose of inferring cloud field properties that it will not be discussed further. More detailed information on why specific rating values were assigned may be found in Appendix A.

The dropsonde deployment mode offers limited potential for deducing the desired cloud information; note ratings between 22 and 45 out of a possible 110. The biggest disadvantage of the dropsonde mode is its sampling limitations. In essence, to deduce an unambiguous cloud top or cloud base height, the radiometer must fall through the cloud. A near miss could result in completely misleading information. However, if a sufficient number of dropsondes were deployed in a given area, these sampling deficiencies could largely be overcome.

Although the RPV solar and infrared deployment modes yield similar ratings (80 to 84; 73 to 82, respectively), the development of an infrared capability seems essential to have a 24 hour capability. The solar radiometer yields more detailed information about the size of cloud elements in the remote mode and this largely accounts for its slightly

higher ratings. However, in any RPV deployment mode, the cost of the

passive radiometric sensors is going to be trivial compared with the

carrier vehicle and associated telemetry; therefore, it is a natural

conclusion that the RPV would carry both solar and infrared radiometers

to optimize cloud field information.

8. RECOMMENDED DEPLOYMENT MODES FOR MAXIMIZING CLOUDINESS INFORMATION
FROM PASSIVE RADIOMETRY

The following recommendations are based upon a composite of hard
and soft information. The hard information is essentially summarized
in this report and consists of physically sound technique development,
specific applications to previously collected data, an attempt to
quantitatively compare the merits of the individual deployment
mode options and experience in the actual deployment of "expendable"
type hardware. The soft information is based upon years of experience
of conducting and analyzing broadband radiometer observations from ground,
balloon and aircraft platforms. This soft information enables one to
intuitively evaluate yet untried schemes relative to their probable
success.

If limited to a single platform for deployment there is no
question that the RPV (remotely piloted vehicle) flying at a number
of flight levels over a reconnaissance area will provide the most and
highest reliability cloudiness information. Optimumly, the RPV would
be instrumented with both upward and downward looking broadband solar
and broadband infrared detectors. Table 1 lists the extent and
variety of information available from such a deployment mode. The
dual spectral capability assures minimum ambiguity; the RPV overcomes
most areal sampling problems associated with other deployment modes;
cloudiness information may be derived from either single altitude or
multiple altitude sampling legs.

The addition of a dropsonde radiometer device to the RPV mode
would be the optimum broadband radiometric cloudiness configuration.
Low clouds or fog could be determined along with increasing reliability
of cloud top height from the RPV alone. However, the dropsonde mode

35

by itself is severely limited by the areal sampling capability of a single unit. Only if multiple sondes were deployed into a single reconnaissance area could one expect to derive reasonably representative cloudiness information.

The least attractive deployment mode for broadband radiometry is the surface implantation concept. Besides the sampling problem associated with a point measurement, the surface implant radiometer would have to be deployed such that vegetation would not impede its line of sight in the upward hemisphere. In other words, it would have to be at the same level or above surrounding vegetation or structures. This constraint alone would seem to compromise its value since even if one were to be sure there were no obstructions, the radiometer would be visually obvious and highly vulnerable to detection and neutralization.

One final set of comments on feasibility and reliability is in order. Feasibility of the RPV solar and dropsonde infrared modes has been demonstrated in section 6. Both instruments can clearly be constructed within the cost constraints for an expendable system. The solar dropsonde hardware is relatively simple and there is no doubt that it also will be cost effective. The only piece of hardware that is sufficiently complex to allow some concern about its reliability in an expendable cost context is the RPV infrared instrument. There is no doubt that such an instrument can be constructed and that it will work; the unknown at present, is whether a workable instrument will cost $200 or $2000. Further prototype development is needed in this case.

APPENDIX A. EXPLANATIONS OF QUANTITATIVE ASSESSMENT FACTORS (SEC. 7)

A1. The single altitude deployment of the multi-sensor instrument will
     enable effective sky cover determinations beneath a/c altitude
     along the slant path(s) represented by each detector (8).

A2. Cloud top altitude may be best deduced from delay times between
     detector traces for detectors aligned in the vertical plane through
     the aircraft's longitudinal axis (8).

A3. Cloud base altitude can be inferred from subtracting cloud height
     plus cloud-aircraft separation from aircraft altitude (6).

A4. Horizontal dimensions of clouds can be determined from pulse width
     of detectors oriented perpendicular to the longitudinal axis of the
     aircraft (9).

A5. The second horizontal dimension of clouds may be inferred from
     detectors not in the vertical plane through the aircraft's longi-
     tudinal axis and not perpendicular to the aircraft's longitudinal
     axis (5).

A6. The areal sampling is limited only by the amount of time available
     to collect the data or the permissible time over target area (10).

A7. Individual cloud statistics are retrievable from all detectors;
     these statistics include mean cloud width, height, spacing, bright-
     ness, background brightness signature, etc. (10).

A8. The sampling time required is the same as that for the aircraft to
     overfly the target area; thus it becomes dependent upon the size of
     the target area and the altitude of the aircraft -- both controllable
     factors (10).

A9. This method of deployment offers maximum flexibility since the air-
     craft may be deployed to a target area of arbitrary specificity and
     the airspace available for the aircraft to overfly (8).

A10. For the amount of data available from a single instrument this method
     of deployment is very cost effective (10).

A11. The most obvious limitations of the solar array configuration are
     the following: daylight only operation; relatively high cloud top
     background brightness contrast (-4).

B1. Multi-level operation will permit more detailed information on sky
     cover stratified by different levels (10).

B2. Cloud top height determinations from different altitudes may be
     inter-compared to determine overall consistency using both
     direct and indirect modes (10).

A-1

B3. Cloud base height determinations may be observed more directly by differencing sky cover determinations at different levels, as well as, using the direct observation mode. (9)

B4. Same as A4. (9)

B5. Same as A5. (5)

B6. Same as A6. (10)

B7. Same as A7. (10)

B8. Sampling time will necessarily increase over A8 since multiple levels of observations are required. (7)

B9. Flexibility is slightly enhanced over A9 since, with some assumptions one could fly different headings at different altitudes and obtain a more continuous distribution of cloud statistics. (9)

B10. In view of increased time over target area for the multiple level observations, this tactic is slightly less cost effective than A10. (9)

B11. The limitations are the same as A11. (-4)

C1. Cloud cover estimates might be deduced if a sufficient number of drops were made so that an adequate portion of the area of interest would be sampled. However, from a single, or a few drops, cloud cover estimates are likely to be unreliable. (1-8)

C2. Provided that a cloud is intersected on descent its top height will be detectable. (7)

C3. Cloud base inference would require information on the angular variation of the solar radiance. (3)

C4. No information. (0)

C5. No information. (0)

C6. Makes only point observations; sampling problems similar to that noted in C1 unless multiple sounds are committed. (1-10)

C7. No information. (0)

C8. Takes multiple drops descending @ 1000' min. (5)

C9. Ballistic trajectory limits flexibility. (5-8)

C10. Relatively low cost per instrument ($5-10) yields instrument costs in the expendable category. (5)

C11. The areal sampling limitations of individual instruments and the daytime only operation account for the negative rating in this category. (-5)

D1. Works best when using eclipse of direct solar beam by clouds; thus limited sample and lengthy time integration necessary. (5-8)

D2. Information simply not retrievable. (0)

D3. Cloud base height may be retrieved from clouds advecting over instrument in the principal plane. (5)

D4. Limited sample available on clouds noted in D3. (5)

D5. Information not retrievable. (0)

D6. Obtains extremely local sample. (4-6)

D7. Very limited statistical sample available. (1)

D8. Lengthy integrations necessary because of reliance on clouds advecting through the principal plane. (1-3)

D9. Stationary detector. (0)

D10. Relatively low cost single instrument outlay, however, there would be virtually no possibility for reuse. (4-2)

D11. The most serious limitations are the following: extremely limited sample of cloud information; performs only in daylight hours; yields no cloud top height information; extremely local observation due to stationary configuration. (-10 - -6)

E1. Thresholding infrared effective temperatures should enable determination of sky cover in all but nearly isothermal and strong temperature inversion cases. (8)

E2. Cloud top effective temperature can be inferred directly from the infrared observations. (9)

E3. No cloud base height information available. (0)

E4. From relatively low resolution sensors individual cloud properties will be difficult to infer; cloud field properties may be more tractable. (2)

E5. Not available. (0)

E6. Excellent sampling capability limited only by slight constraints of aircraft. (10)

A-3

E7. Individual cloud statistics will be difficult; a less detailed summary of cloud field equivalent brightness or height statistics will make-up for this in part. (6)

E8. Same as A8. (10)

E9. Potentially offers more flexibility than solar detectors since larger field of view detectors will be less dependent upon specific flight heading chosen. (8)

E10. Same as A10. (10)

E11. In spite of the detailed cloud statistics not being available from this type of deployment, the day/night capability of this system earns a bonus (or negative penalty points) in this category. One cautionary note, however is that this technique will not perform with either a temperature inversion or constant temperature layer beneath the aircraft. (10)

F1. Multiple altitudes improve confidence in sky cover information and allow for some relative calibration from direct observations. (10)

F2. Same as G1. (10)

F3. Some cloud base information may be obtainable by differencing sky cover amount between two levels as well as by direct observation. (8)

F4. Same as E4. (2)

F5. Same as E5. (0)

F6. Same as E6. (10)

F7. Same as E7. (6)

F8. More flight levels increase data acquisition period. (8)

F9. Same as E9. (9)

F10. Additional flight levels increase cost. (9)

F11. Same as E11. (10)

G1. Same as C1. (2-8)

G2. Same as C2. (8)

G3. Cloud base height determination will depend on temperature difference between underlying surface and cloud base. (4)

G4. Same as C4. (0)

G5. Same as C5. (0)

G6. Same as C6. (1-10)

G7. Same as C7. (0)

G8. Same as C8. (5)

G9. Same as C9. (5-8)

G10. Same as C10. (5)

G11. Areal sampling limitations of individual instruments account
     for negative rating. (-3-0)

APPENDIX B.   PRELIMINARY DECIGN AND FABRICATION
MOCKUPS OF INEXPENSIVE INFRARED INSTRUMENT

A laboratory version of an inexpensive infrared instrument
designed to make the broadband infrared measurements alluded to in
Sections 4.121, 4.122 and Appendix D is illustrated in Figures B1,
B2 and B3.   The instrument has been designed around a relatively
inexpensive pyroelectric detector with a filter band-pass of 7-14 μm.
Figure B1 shows the body of the instrument machined out of plastic
with a pneumatic chopper drive in place.   There are four detector
mounting holes oriented at appropriate angles for the observations.
Chopper position sense switches are installed at the locations where
the wires terminate in the plexiglass block.   Figure B2 shows the same
assembly with the aluminum chopper plate in a closed position and Figure
B3 shows the fully assembled instrument.

Figure B4 shows the geometric collimator - detector assembly.
The pyroelectric detector is shown on the lower left.   The small
discs with the holes and the short cylinders fit inside the longer
cylinder to provide appropriate collimation.   The detector assembly
fits in one end of the longer cylinder.

Figures B5 and B6 show a block diagram of the readout electronics
and a diagram of the readout circuit, respectively.

At the termination of the present contract, fabrication of the
elements of the IR detector scheme was completed; insufficient time and
resources were available to do extensive testing.   However, superficial
testing to date does not give us any reason to doubt the ability of
the basic design features outlined above to yield the information
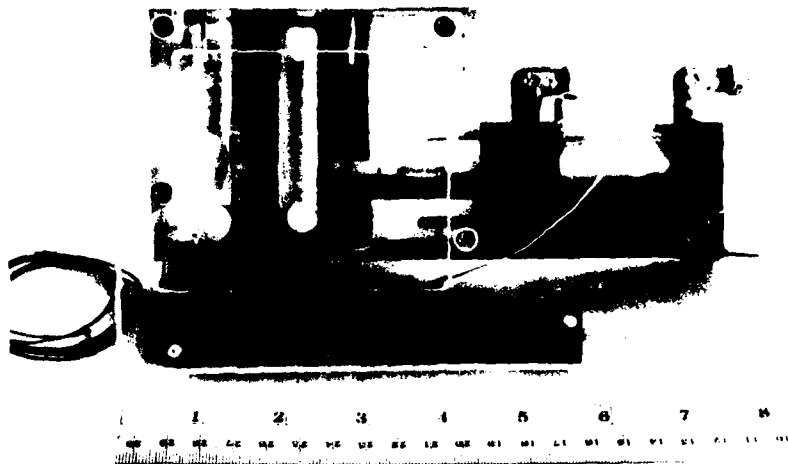required to infer cloud field properties.

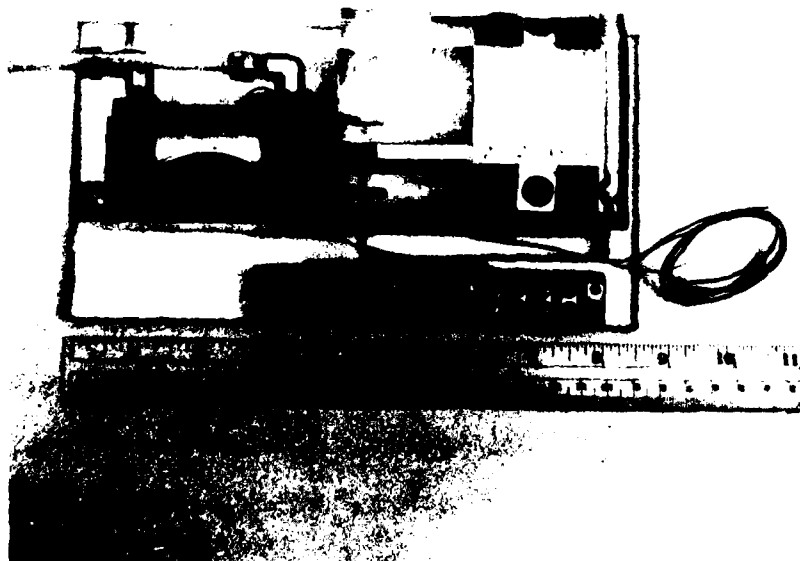Figure B1. Basic Instrument Body

Figure B2. Basic Instrument Body with Aluminum Hopper Plate
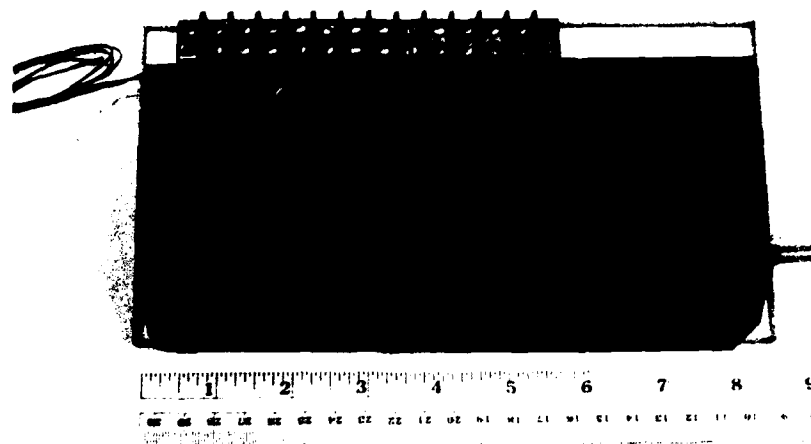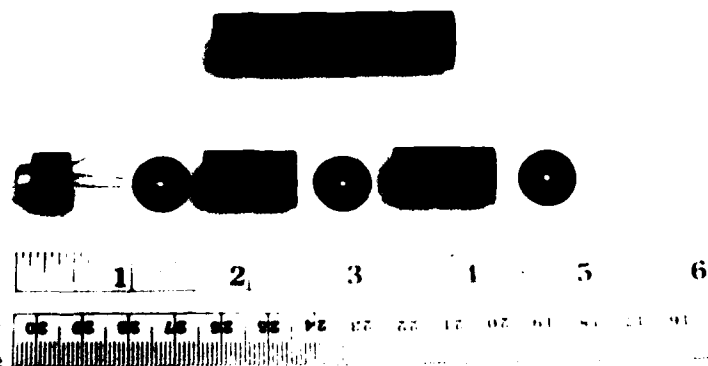
Figure B3. Basic Instrument Completely Assembled

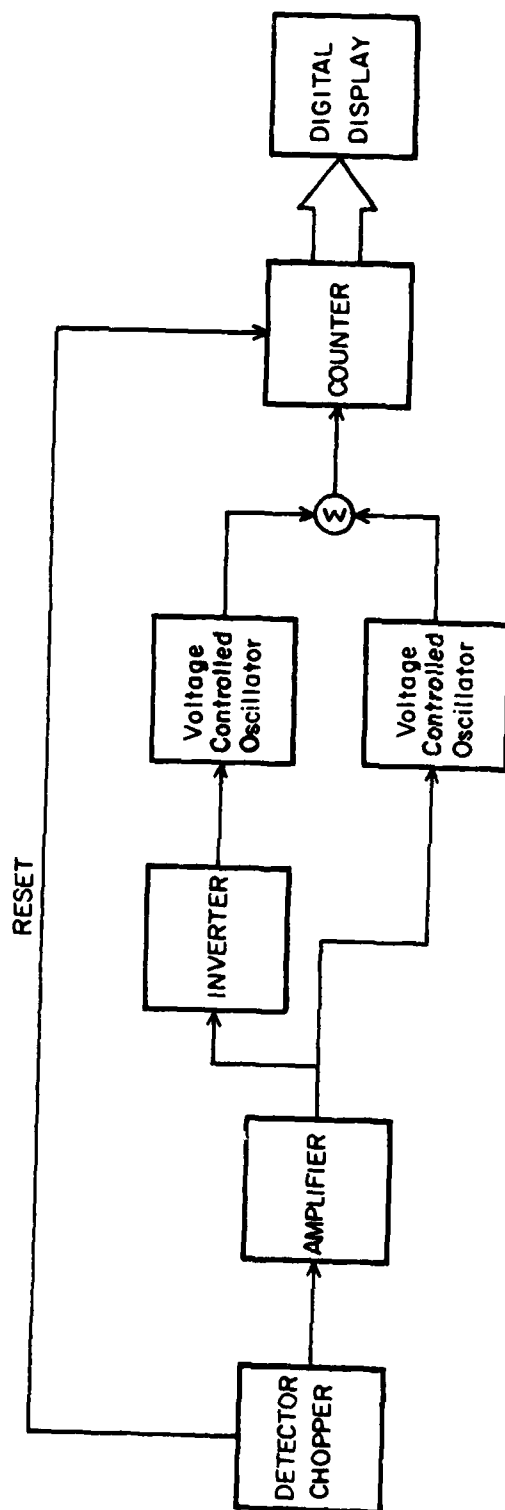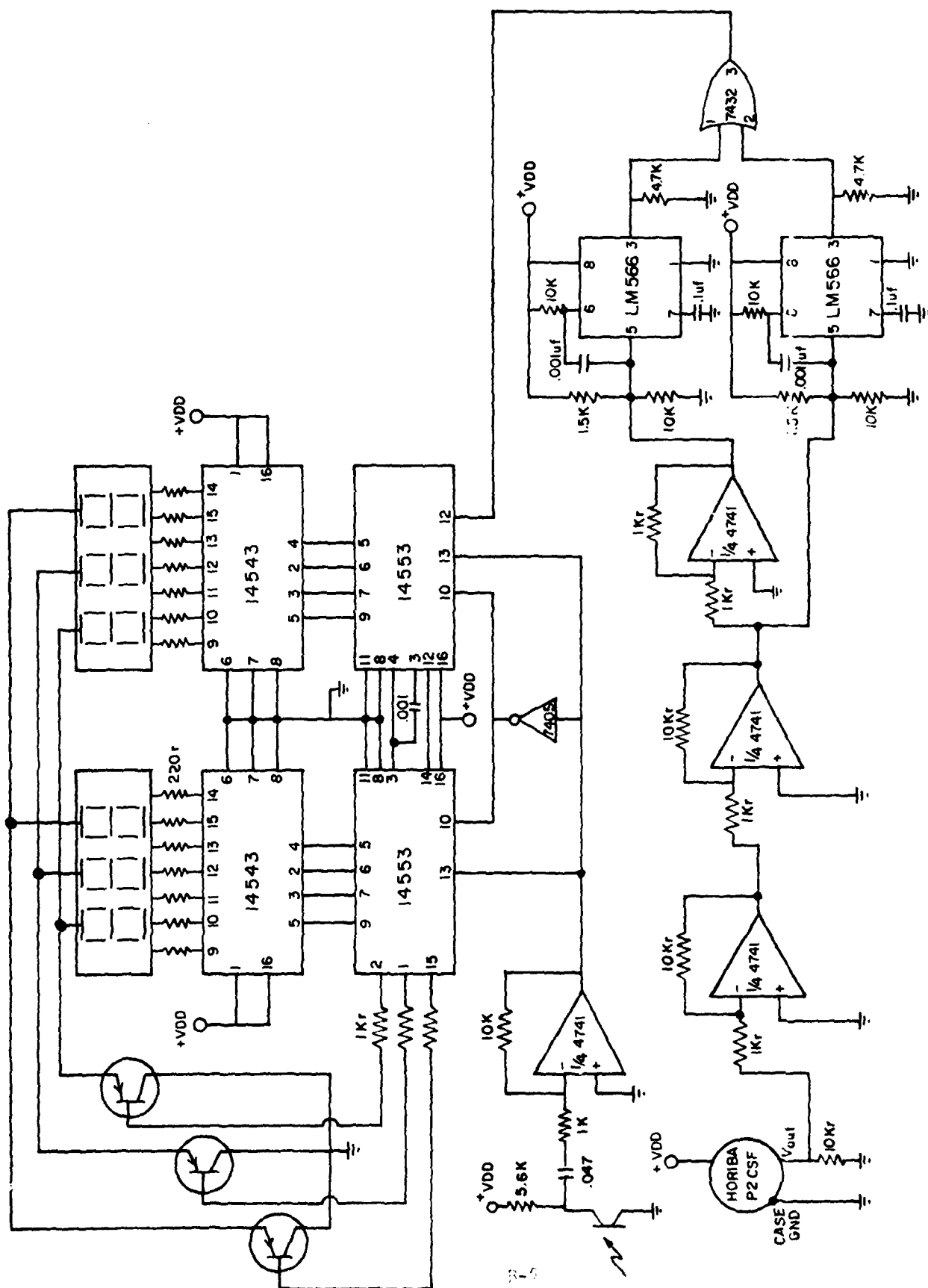Figure B4. Geometric Collimator and Pyroelectric Detector

Figure 5. Block Diagram of the Readout Electronics Circuit

Figure 6. Block Diagram of the Readout Circuit

APPENDIX C

Comparison of Satellite and All-Sky Camera Estimates of Cloud Cover during GATE

STEVEN A. ACKERMAN AND STEPHEN K. COX

Department of Atmospheric Science, Colorado State University, Fort Collins, 80523

(Manuscript received 31 July 1980, in final form 24 November 1980)

ABSTRACT

Horizontal cloud coverages derived from a geostationary satellite and all-sky cameras were compared for a 3-month period of the GARP Atlantic Tropical Experiment (GATE). Estimates of total cloud cover using the satellite and all-sky camera were similar for the daytime period. The all-sky cameras also gave reasonable estimates of the 24 h cloud cover due to the small difference in the satellite determined daytime and nighttime total cloud cover in the vicinity of the all-sky cameras. However other regions in the area of study which were not covered by an all-sky camera revealed large diurnal variations. In these areas the daytime total cloud amount did not yield an accurate representation of the 24 h cloud cover.

A method is presented which enables one to construct a three-dimensional representation of cloud structure by combining surface and satellite observations. The disadvantages of this technique are that it assumes no overlapping cloud tops or cloud bases, as well as the limitations of the satellite and all-sky camera in estimating cloud cover.

1. Introduction

Observations of cloud amount and type are an important tool in weather forecasting and climatological studies. Before the age of satellites, cloud amounts and cloud types were observed and recorded routinely at ground-based observatories. With the coming of operational satellites, clouds may now be observed from both ground-based and satellite platforms.

Each method has its advantages and disadvantages. The long record of man's observations of clouds has made cloud classification from the ground routine. Ground-based observations of clouds generally include the type, stratification, amount, opacity, direction of movement and cloud-base height. In general, cloud observations from the ground are somewhat subjective, especially in estimating cloud amount. Cloud-base height can be roughly estimated based on the cloud type. A better estimation of cloud base height may be obtained by using a rotating-beam ceilometer, a balloon, rawinsonde, radar, reference altitude, etc. Ground-based observations, although limited in the horizontal extent, have very fine spatial resolution. The high spatial resolution can aid in discerning multilayered clouds. Multilayered clouds can also be detected visually provided the lower cloud is not opaque. Observations taken at night are much more limited than the daytime observations.

Although very fine spatial resolution is lost in the satellite observation, the horizontal extent of coverage may be global. Cloud classification by the satellite is not as refined as the ground-based observa-

tion. Observations of cloud sides by a satellite can be interpreted as cloud tops. Cloud classification is generally limited to assigning a cloud-top height based on an infrared (IR) *brightness temperature* in conjunction with a vertical temperature and moisture profile. A disadvantage of this technique is that cloud-top assignment of thin clouds with emittances < 1.0 are misplaced at a lower height. During the daylight hours observations in the visible spectrum by the satellite aid in identifying cloud types. *Errors in cloud-top location result from several assumptions regarding instrument resolution, cloud microphysical structure as well as the state of the atmosphere above the cloud.*

Recognizing the advantages and disadvantages of both the ground-based and satellite-derived cloud cover information, cloud-cover estimates from the two different platforms are compared. Since the satellite observes the cloud field from the top of the atmosphere while the ground-based observations view the field from the bottom, comparisons are somewhat limited. However, these complementary perspectives have the advantage of enabling one to estimate a three-dimensional cloud structure. Such a technique is proposed in this paper.

2. Comparison of ground-based and satellite-derived cloud-cover estimates

During the summer of 1974 the GARP[1] Atlantic Tropical Experiment (GATE) was executed to investigate weather systems of western Africa and the

___
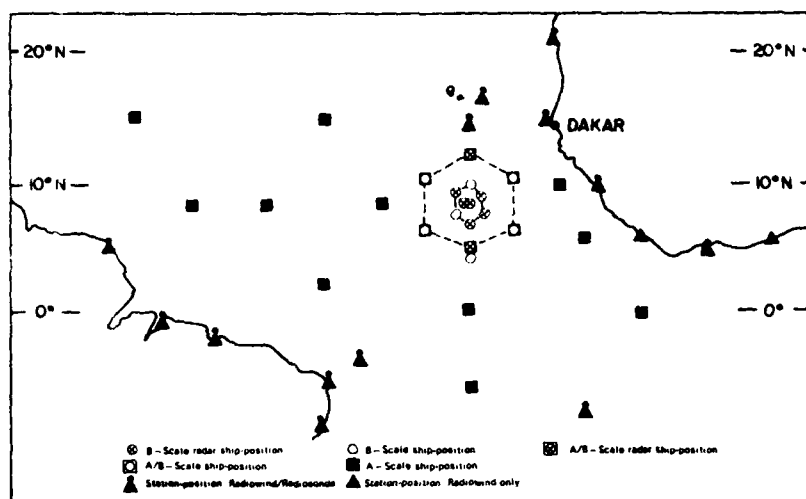[1] Global Atmospheric Research Program.

FIG. 1a. Ship positions during Phase III of GATE.

eastern Atlantic (Fig. 1a). During this regional experiment atmospheric and oceanic data were collected from a variety of platforms on land, ship, aircraft and satellites. The GATE was divided into three periods of intensive observation. The dates of these periods are Phase I: 28 June–16 July;

FIG. 1b. Graphical depiction of A-B- and B-scale arrays during Phase III of GATE. Dashed lines enclose ½ latitude by ½ longitude boxes, solid lines represent geographical latitude and longitude. Integer values centered within dashed boxes represent numbering scheme used in identifying specific areas.

Phase II: 28 July–17 August; and Phase III: 30 August–19 September. During this experiment four U.S. vessels were equipped with all-sky cameras to investigate the interactions of clouds and the tropical atmosphere. In addition, the Synchronous Meteorological Satellite-1 (SMS-1) was available for radiometric measurements and cloud observations.

Recently Holle et al. (1979, hereafter referred to as HSL) analyzed data from the four U.S. ship all-sky cameras for the GATE B-scale array (Figs. 1a and 1b). A Bolex H-16 camera took 16 mm color exposures every 15 s during the daylight periods of GATE. The field of view of the camera was 197°. However, due to obstruction by other instrumentation, the field of view analyzed varied between 115 and 142°, depending on the ship. HSL projected the 617 280 panoramic photographs onto a linear grid and estimated cloud cover amounts for each day of the experiment. Distance between the ships was typically 150 km so that there is no overlapping of the photographs. Hence, each all-sky camera observation is independent. As part of their study, HSL present phase averages of high, low and total cloudiness for each vessel.

Cox and Griffith (1979a, b, hereafter CG) generated cloud-top amounts for the three phases of GATE using the 10.5–12.5 μm infrared (IR) channel of the Visible and Infrared Spin Scan Radiometer (VISSR) SMS-1 satellite. The maximum resolution of this instrument is ~7 km. Cloud-top percent areal coverages for 100 mb intervals (100 mb–surface) were derived for each ½° latitude by ½° longitude area element within the A/B array (Fig. 1b). The ½° box averages were then composited with respect to various temporal and spatial intervals. Cloud-top heights were derived from the satellite IR blackbody temperatures in conjunction with
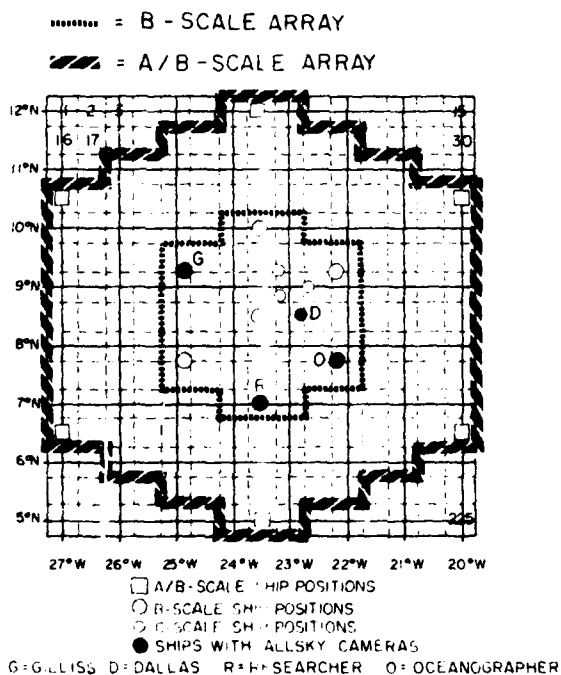
an appropriate temperature profile. Visible satellite data were used to verify the IR threshold value of clear skies. To better estimate a true cloud top pressure, two corrections were applied to the satellite derived IR blackbody temperature. The first correction term accounts for the water vapor emission in the "window" (10.5–12.5 μm) region that the satellite senses. This correction is dependent on the total precipitable water in the atmosphere, its vertical distribution and the temperature profile. This correction term is of primary importance for pressures > 500 mb. The second correction term adjusts the finite penetration distance into the cloud before radiative "blackness" is achieved. This distance is a function of the cloud water/ice content and the mass absorption coefficient and typically increases with decreasing pressure.

From the phase averages derived in HSL and CG it is possible to compare ground- and satellite-based observations of cloud amount. Fig. 2 shows the contoured phase-average total cloud-cover amount maps derived as a by-product from the radiative divergence profiles produced by CG. The left-hand portions of the figure are reproductions of the maps produced by HSL. The area shown in the right-hand portion of the figure was scanned by the satellite-borne radiometer and is obviously larger in areal extent than the HSL maps. It is plain to see that the satellite data provide more detailed information than the smaller area mapped by HSL which is shown as a box in the CG analysis. HSL use data only from the four ships shown in the figure and subjectively interpolate between them to produce their contours. The satellite data grid has many more point sources, 225 in all (Fig. 1b) and, consequently, more objective contouring may be performed.

Agreement between the two techniques is expected when comparing total cloudiness since each cloud base has a cloud top and vice versa. Disagreement between the techniques should be a result of the different spatial and temporal resolutions as well as the "cloud–no cloud" definition. The agreement during Phase I between the data provided by the two platforms is quite striking. Discrepancies between the satellite versus camera derived total cloud amounts are less than 5% at each of the four ship locations. Analysis of the all-sky camera derived cloud amounts indicates a cloud band, the Intertropical Convergence Zone (ITCZ), oriented east-west. The satellite data indicate that the ITCZ is oriented east-northeast to west-southwest. Agreement in Phase II is not quite as good as in Phase I. Although the total cloud cover determined in the vicinity of the ships *Dallas* and *Researcher* for the two data sets agrees well, there is disagreement at the *Oceanographer* and *Gillis* locations where there is a relative mini-
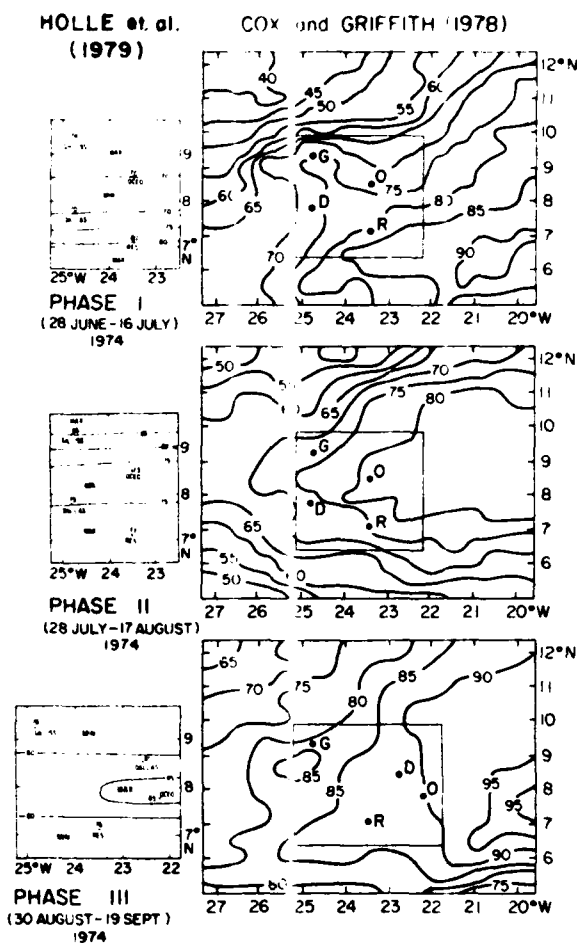

HOLLE et. al. (1979)   COX and GRIFFITH (1978)

PHASE I
(28 JUNE – 16 JULY)
1974

PHASE II
(28 JULY – 17 AUGUST)
1974

PHASE III
(30 AUGUST – 19 SEPT)
1974

FIG. 2. A comparison of total cloud amount contours (%) during each phase of GATE derived from Holle *et al.* (1979) and Cox and Griffith (1978).

mum in the HSL analysis while CG show a relative maximum. Both studies show a northward progression of the ITCZ between Phases I and II. The satellite analysis presents a better definition of the ITCZ boundaries. Phase III spatial gradients in total cloud cover between the four ships agree in the two studies, with the absolute values of total cloudiness being consistently larger by 5–10% in the CG data set.

HSL vertically stratified the clouds as low, middle or high depending on the cloud-base location. Observations from the top of the atmosphere classify low, middle or high cloud as a function of cloud top. Fig. 3 presents a comparison between the maps produced from the two data sources for Phase III. The top portion of the figure shows the cloudiness that CG characterize as low, the lower portion shows the high clouds. Because of obscuration of low clouds by higher clouds, one would expect the
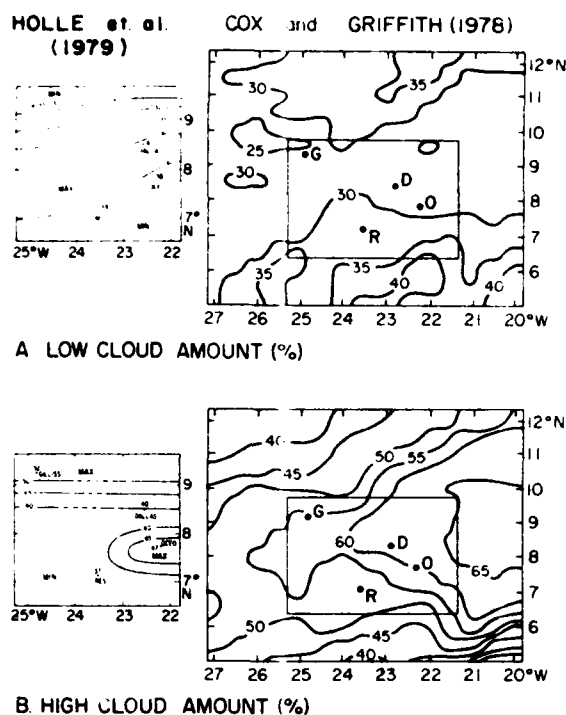
HOLLE et al.   COX and GRIFFITH (1978)
(1979)

A LOW CLOUD AMOUNT (%)

B HIGH CLOUD AMOUNT (%)

FIG. 3. GATE Phase III low and high cloud amounts for satellite and surface area determination for 0600 -1800 GMT.

amount of low clouds deduced from satellite data to be less than the low cloud amounts generated from surface observations. In the case of the high cloud classification the satellite determined amount should be larger than that of the ground-based platform. Fig. 3 agrees with these expectations. One notes that by using time-lapse photography HSL could estimate high cloud amounts even when there was obscuration of these clouds by lower clouds. In addition, HSL could discern high thin clouds that might be misinterpreted by the satellite analysis as a middle-level cloud. These advantages of the all-sky camera can be used to refine the technique for inferring a three-dimensional cloud structure developed later in the text.

One obvious limitation of using all-sky camera photography to assess cloud cover amounts is that between dusk and dawn no data are collected. For this reason the foregoing comparisons have been restricted to the daytime hours, i.e., 0600 – 1800 GMT Cox and Griffith (1978, hereafter CG78) use infrared satellite data to generate cloud-cover information, consequently daily (24 h) cloud-cover amounts can be calculated and the diurnal variability in cloudiness can be monitored.

Fig 4 shows the mean nighttime (1800–0600 GMT) total cloud cover amounts for Phase III of the GATE derived from the CG78 data set and the

complementary daytime map. The figure shows that in the mean the Phase III total cloud cover for the A/B array is greater during the nighttime period, and that the horizontal gradients are slightly less at night. As a result of the small difference between the daytime and the nighttime total cloud cover at the four ship positions, the effect of including the latter in determining a 24 h time-average cloud-cover composite appears to be small at these locations. However, diurnal variations of other geographical regions within the array are as large as 25%. In these regions an all-sky camera would not yield an accurate representation of the 24 h cloud cover. The total cloud cover amounts presented in Fig. 4 are averaged over the 20-day Phase III period, thereby smoothing out any large-scale day-to-day synoptic changes. Diurnal variations of cloud cover on a day-to-day basis would undoubtedly show variations that are larger than 25%. Analysis of the diurnal variation in total cloud cover for Phases I and II yield similar results.

3. Cloud vertical structure

Until recently, large-scale estimates of cloud cover have primarily been based on satellite observations of cloud top. To obtain a vertical structure of the cloud field it is necessary to assign a cloud-base distribution. Dopplick (1972)
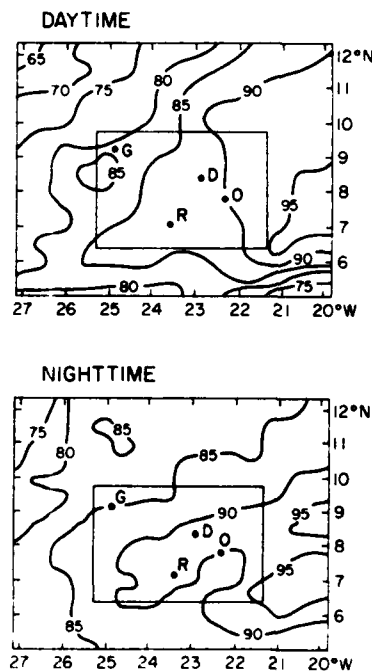
DAYTIME

NIGHTTIME

FIG. 4. Daytime (0600 1800 GMT) and nighttime (1800 0600 GMT) mean total cloud cover.

TABLE 1. The convective state of the atmosphere as a function of the GATE convective cloud code.

Code	Convective state
1	Extremely depressed convection
2	Slightly depressed convection
3	Weakly enhanced convection
4	Moderately enhanced convection
5	Strongly enhanced convection

parameterized cloud structure by assuming a constant cloud thickness, with no overlapping clouds. While Cox and Griffith (1979a, b) and Ackerman and Cox (1980) parameterized cloud structure by allowing only thin and thick clouds, again, with no overlapping cloud tops. Thin clouds were defined as having cloud base within the same 100 mb layer as the cloud top. For the "thick" clouds, cloud base was assumed at 950 mb, the approximate lifting condensation level of the GATE region. The distribution of thin and thick clouds was based on a correlation between areas of precipitation (thick clouds) and satellite-derived cloud-top temperatures.

Another possible method of determining vertical cloud structure during GATE is by using some of the tabulated data given by Holle et al. (1977). A GATE convective code was adopted from Garstang and Aspliden (1974) as a method of classifying the convective state of the atmosphere at the time of the observation. Each convective code number was to be assigned on the basis of a given radar pattern, cloud distributions and vertical profiles of temperature, humidity and equivalent potential temperature. Table 1 lists the convective state of the atmosphere corresponding to an assigned convective code number. Using all-sky cameras, Holle et al. (1977) correlated a convective code with four categories of observed cloud base: low, middle, upper undifferentiable and high. It is a difficult task to correlate convective activity with satellite imagery. However, once such a relationship is established, the method described below can be used to determine the vertical structure of clouds, again, assuming no multilayered clouds. Fig. 5 shows the type of cloud struc-

ture assumed and the notation used in the text. The first capital letter denotes cloud top when combined with a subscript which denotes cloud base, thus, H_H represents a high-cloud top with high-cloud base. When the capital letter is combined with a superscript the first denotes cloud top when the superscript is T, and it denotes cloud base when the superscript is B. Thus, H^T represents a cloud with a high top.

From satellite data, one can obtain the percent of clouds with low tops (L^T), middle tops (M^T), and high tops (H^T). From the all-sky camera data of Holle et al. (1977) the percent areal coverage of clouds with low bases (L^B), middle bases (M^B) and high bases (H^B) as a function of convective code, is known.

The percentage of clouds with low tops and low bases (L_L) is simply the percent of low tops determined from the satellite images (L^T). Similarly the amount of clouds with high tops and high base (H_H) is the percentage of high bases (H^B) determined from the all-sky camera. That is,

$$L_L = L^T \quad \text{and} \quad H_H = H^B. \tag{1}$$

Thus

$$L^B = L^B - L^T \quad \text{and} \quad H^T = H^T - H^B. \tag{2}$$

where L^B denotes the total percentage of clouds with low bases that is to be distributed among M_L and H_L, and H^T is the percent of clouds with high tops to be distributed among H_L and H_M. One can derive a set of three equations [Eqs. (3)–(5)] with four unknowns: M_L, M_M, H_L and H_M

$$M_M + M_L = M^T, \tag{3}$$

$$H_L + H_M = H^T, \tag{4}$$

$$M_M = H_L \quad M^T - L^B. \tag{5}$$

By parameterizing one of the unknowns, the remaining three can be solved. The percent coverage of H_L is parameterized based on a radar-satellite analysis described in CG. H_M and M_M are solved by use of Eqs. (4) and (5), respectively. Eq. (3) can then be used to solve for M_L.

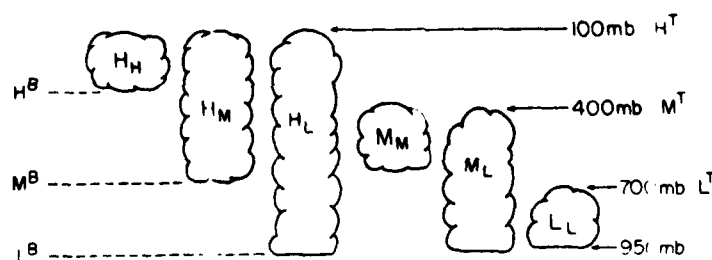CG have derived a mean cloud-top distribution for

FIG. 5. Schematic view of assumed cloud structure. For explanation of notation see text.

TABLE 2. Three-dimensional cloud structure for suppressed and enhanced convection during Phase III of GATE.

Cloud type	Suppressed convection	Enhanced convection
H_H	9.8	24.8
H_M	0	0
H_L	0	8.2
M_M	33.8	7.4
M_L	0	27.1
L_L	35.2	24.1
Clear	21.2	8.4

suppressed and enhanced convective activity during Phase III of GATE. Assuming that the cloud-base distribution of convective code 1 is representative of suppressed convection while enhanced convection cloud base distribution is represented by codes 4 and 5, the vertical cloud distribution can be derived as discussed above. These cloud structures are given in Table 2 Note that the cloud-top pressure levels in the present study are only distributed within three pressure intervals (see Fig. 5). The results listed in Table 2 indicate that suppressed convection during Phase III of GATE consisted mostly of middle and lower atmospheric cloud layers. In the case of enhanced convection there is much more total cloudiness than for the suppressed convection. Although there is an apparent decrease in the amount of low cloud (L_L) in the enhanced convection case, there is a substantial increase in the cumuliform cloud types H_L and M_L. The large increase in the amount of these cloud structures indicates a vertical transport of moisture from the lower atmosphere to the middle and upper troposphere. This transport is not suggested by the suppressed convection cloud structure. The increase in the amounts of high cloud tops with high cloud bases (H_L) reflects the cirrus outflow of the enhanced convection.

Due to the large differences in the viewing angle between the satellite and the four all-sky cameras, cloud systems that are detected by the satellite may not be viewed by the all-sky cameras. Averaging the cloud top and base percent coverages over the entire Phase III period reduces this sampling error in the determination of cloud vertical structure given in Table 2 The technique discussed above for determining cloud structure is most accurate when the satellite view is coincident with the all-sky camera.

When the satellite and all-sky camera are centered on the same location, discrepancies in determining cloud amount are due to the limitations of each method. The first of these limitations is the satellite's maximum spatial resolution which, in the present study, is 7 km. The resolution of the all-sky camera (human eye) can be on the order of meters. This very fine spatial resolution can aid in resolving overlapping cloud bases. Multilayered clouds may

also be estimated from time-lapse photography. Although not included in the present study, use of the all-sky camera's ability to portray the amount of overlapping cloud bases, may refine the determination of a three-dimensional cloud structure. As discussed previously the satellite incorrectly assigns the cloud tops of thin clouds to a lower altitude. Use of the all-sky camera may aid in the detection of thin cloud amounts, at least on a case study basis. The major disadvantage of the all-sky camera is its limited areal coverage. For this reason cloud base distribution was parameterized as a function of convective code. However, for case studies employing single ship observations such a parameterization may not be necessary.

4. Summary

Horizontal cloud averages derived from satellite and all-sky camera data were compared for the three Phases of GATE. While the comparisons of all-sky camera derived cloud amounts versus the satellite derived cloud amounts in the vicinity of the four ships with all-sky camera equipment was excellent during Phase I, agreement between the two techniques was within 10–15% for Phases II and III. Cloud cover estimates determined from the satellite had a larger areal coverage and a higher two dimensional data density than the four all-sky cameras, allowing gradients in the horizontal total cloud cover to be defined more reliably. The phase mean diurnal variation in the satellite determined total cloud cover over the four ships was small, thus the all-sky camera gave reasonable estimates of the 24 h total cloud cover. However, other geographical regions within the area of study which are not covered by the all-sky camera reveal large diurnal variations. In these areas the daytime total cloud amount, and hence an all-sky camera, does not yield an accurate representation of the 24 h cloud cover. The mean diurnal variations in cloud cover discussed above are a composite over ~20 days. The extent to which a daytime cloud amount observation is representative of a 24 h cloud-cover amount is inevitably a function of the temporal average as well as the geographical location of the observation.

As a result of the opposing view angles of the satellite and all-sky camera with respect to a given cloud field, the two observations may be combined to estimate the three-dimensional cloud structure. This method is presented and applied to derive the cloud structure of suppressed and enhanced convection during Phase III of GATE. The disadvantages of this technique are that it assumes no overlapping cloud tops or cloud bases, as well as the individual limitations of the satellite and all-sky camera in determining cloud cover estimates.

REFERENCES

Ackerman, S. A., and S. K. Cox, 1981: GATE Phase III mean synoptic-scale radiative convergence profiles. *Mon. Wea. Rev.,* **109,** 371–383.

Cox, S. K., and K. T. Griffith, 1978: Tropospheric radiative divergence during Phase III of the GARP Atlantic Tropical Experiment (GATE). Atmos. Sci. Pap. 291, Colorado State University, Ft. Collins, 166 pp. [NTIS PB292761].

——, and ——, 1979a: Estimates of radiative divergence during Phase III of the GARP Atlantic Tropical Experiment, Part I: Methodology. *J. Atmos. Sci.,* **36,** 576–585.

——, and ——, 1979b: Estimates of radiative divergence during Phase III of the GARP Atlantic Tropical Experiment, Part II: Analysis of Phase III results. *J. Atmos. Sci.,* **36,** 586–601.

Dopplick, T. G., 1972: Radiative heating of the global atmosphere. *J. Atmos. Sci.,* **29,** 1278–1294.

Garstang, M. A., and C. I. Aspliden, 1974: Convective cloud clode. Dept. Environ. Sci., University of Virginia, Charlottesville, 20 pp.

Holle, R. L., S. W. Leavitt, J. Simpson, R. Biondini and J. W. Snow, 1977: Cloudiness from whole-sky pictures taken aboard four U.S. B-scale ships. Dept. Environ. Sci., University of Virginia, Charlottesville, 110 pp.

——, Joanne Simpson and S. W. Leavitt, 1979: GATE B-scale cloudiness from whole-sky cameras on four U.S. ships. *Mon. Wea. Rev.,* **107,** 874–895.

APPENDIX D. DERIVATION OF RELATION BETWEEN BROADBAND
INFRARED RADIOMETER DATA AND CLOUD COVER

Refer to Section 4.122 for denitions of N_{CLD}; N_{CLR}; N_S; and L.

Let Ω_{CLR}, Ω_{CLD} and Ω_S refer to the solid $\angle$ subtended by clear sky, cloud tops and cloud sides, respectively. θ is zenith angle; ϕ is an azimuthal coordinate.

The total solid angle subtended by all cloud tops, assuming a mean circular cloud top radius r_c and height, h, in a θ, $\theta + \Delta\theta$ annulus is:

$$\Omega_{CLD} = \Sigma\pi r_c{}^2 \; \frac{\cos\overline{\theta}}{\ell^2/\cos^2\overline{\theta}} = \Sigma\pi r_c{}^2 \; \frac{\cos^3\overline{\theta}}{\ell^2} \tag{1}$$

where ℓ is the vertical distance between the observation platform and the cloud top.

The total solid angle of the annulus is:

$$\Omega_{TOT} = 2\pi \sin\theta \, d\theta . \tag{2}$$

Let Q be the fractional amount of cloud cover, (uniformly distributed in θ and ϕ) in the horizontal plane; then;

$$Q = \Sigma \; {\pi r_c{}^2} \Big/ {\pi\ell^2[\tan^2(\theta+\Delta\theta)-\tan^2\theta]} \tag{3}$$

or

$$Q = \Sigma \; {\pi r_c{}^2} \Big/ {\pi\ell^2 \, d(\tan^2\theta)} . \tag{4}$$

Solving (4) for $\Sigma\pi r_c{}^2$ and substituting into yields

$$\Omega_{CLD} = \pi Q \cos^3\theta \, d(\tan^2\theta) . \tag{5}$$

Next for a cylindrical cloud with radius, r_c, and height h, the cross sectional area of a side is

$$A_S = 2r_c h,$$ (6)

and the component viewed from angle θ is

$$A_S' = 2r_c h \sin \theta.$$ (7)

The solid angle subtended by a single cloud is given by

$$\Omega_S = \frac{2r_c h \sin \theta \cos^2\theta(1-h/\ell)}{\ell^2}.$$ (8)

For all cloud side contributions (neglecting obscuration)

$$\Omega_S = \Sigma 2r_c h \frac{\sin \theta \cos^2\theta(1-h/\ell)}{\ell^2}.$$ (9)

Let $\ell \gg h$, then (9) becomes

$$\Omega_S = \Sigma 2r_c h \frac{\sin \theta \cos^2 \theta}{\ell^2}.$$ (10)

Let $\beta = r_c/h$ and assume β is the same for all clouds viewed. Then

$$\Sigma \pi r_c^2 = \frac{\pi\beta}{2} \Sigma 2rh.$$ (11)

Substituting (11) into (4) yields

$$Q = \frac{\beta}{2\ell^2} \frac{\Sigma 2rh}{d(\tan^2\theta)}.$$ (12)

Now solving (12) for Σ 2rh and substituting into (10) yields

$$\Omega_S = \frac{4Q}{\beta} \sin \theta \tan \theta \, d\theta.$$ (13)

Now

$$\Omega_{CLR} = \Omega_{TOT} - \Omega_{CLD} - \Omega_{S}. \tag{14}$$

Then

$$\Omega_{CLR} = 2\pi \sin\theta \, d\theta [1-Q- \frac{2Q\tan\theta}{\pi\beta}]. \tag{15}$$

Now

$$L = N_{CLR} \times \Omega_{CLR} + N_{CLD} \times \Omega_{CLD} = N_S \times \Omega_S. \tag{16}$$

Substituting for Ω_{CLR}, Ω_{CLD} and Ω_S from (15), (1) and (13) respectively, yields

$$L = \int_0^\theta N_{CLR} [2\pi \sin\theta \, (1-Q-\frac{2Q\tan\theta}{\pi\beta}] \, d\theta \tag{17}$$

$$+ \int_0^\theta N_{CLD} [2\pi Q \sin\theta \cos\theta] \, d\theta$$

$$+ \int_0^\theta N_S [\frac{4\alpha}{\beta} \sin^2\theta] \, d\theta.$$

Performing the indicated integrations and solving for Q yields

$$Q = \frac{L - \pi N_{CLR}[1-\cos^2\theta]}{\pi[1-\cos^2\theta][N_{CLD}-N_{CLR}] + \frac{1}{\beta}[2\theta-\sin 2\theta][N_S-1]}. \tag{18}$$

APPENDIX E.   REMOTE SENSING OF CLOUD FEATURES USING PASSIVE
SOLAR RADIOMETRY

Refer to figure 1, section 4.111 for a schematic description of the
variables used in the following equations.

The total pulse width sensed by a detector is:

$$T_{2\ \theta_i} - T_{1\ \theta_i}\ \propto\ \omega_0 + h\ \tan\theta_i \qquad (1)$$

For $\theta_i = 0$, solving (1) for ω_0

$$\omega_0 \propto\ T_{2\ \theta_0} - T_{1\ \theta_0} \qquad (2)$$

Next substituting (2) into 1 for $\theta_i \neq 0$, and solving for h, the
height of the element,

$$h\ \propto\ [(T_{2\ \theta_i} - T_{1\ 0_i}) - (T_{2\ \theta_0} - T_{1\ \theta_0})] \Big/ \tan\theta_i \qquad (3)$$

The cloud top height, ℓ, relative to the aircraft flight altitude
is:

$$\ell \propto [T_{2\ \theta_j} - T_{2\ \theta_i}] \Big/ [\tan\theta_j - \tan\theta_i] \qquad (4)$$

where $\theta_j > \theta_i$.

The constants of proportionality in equations 1-4 are determined by
the speed of the platform relative to the cloud elements; in practice
the airspeed will be sufficient.

For a set of detectors having a side viewing component where α
is the angle between the perpendicular to the center line of the aircraft
and a particular detector equation 1 is modified.

$$T_{2\alpha} - T_{1\alpha} \propto W_0 + W' \tan \alpha \qquad (5)$$

where W_0 is the width dimension of the cloud in the direction along the flight path and W is the width dimension of the cloud perpendicular to the flight path.

For the sensor with $\alpha = 0$

$$W_0 \propto T_{2\alpha_0} - T_{1\alpha_0} \qquad (6)$$

Then from (1)

$$W' \propto \left[T_{2\alpha i} - T_{1\alpha i} - W_0\right] \Big/ \tan \alpha_i \qquad (7)$$

APPENDIX F. AN EXAMPLE OF CONTRACT INFORMATION CONTAINED IN PASSIVE
RADIOMETRY DATA

The figures presented in this appendix are raw data frequency
distributions representing the same features analyzed in section 6.12.
My reason for presenting these data, is to illustrate the detailed
information available from the "cloud detector array" which quantitatively
represents the range of brightness or contrast of a given scene. In
the following cases, a detector with a spectral bandpass between .3
and 1.1 micrometers was used; thus, these frequency distributions are
strongly weighted to the visible wavelengths.

While the following figures represent solar bandpass data, the
same type of information could be generated for other parts of the
spectrum from appropriate arrays of detectors.

This detailed information could be used along with a knowledge
of specific guidance or surveillance requirements to further optimize
ordnance selection.
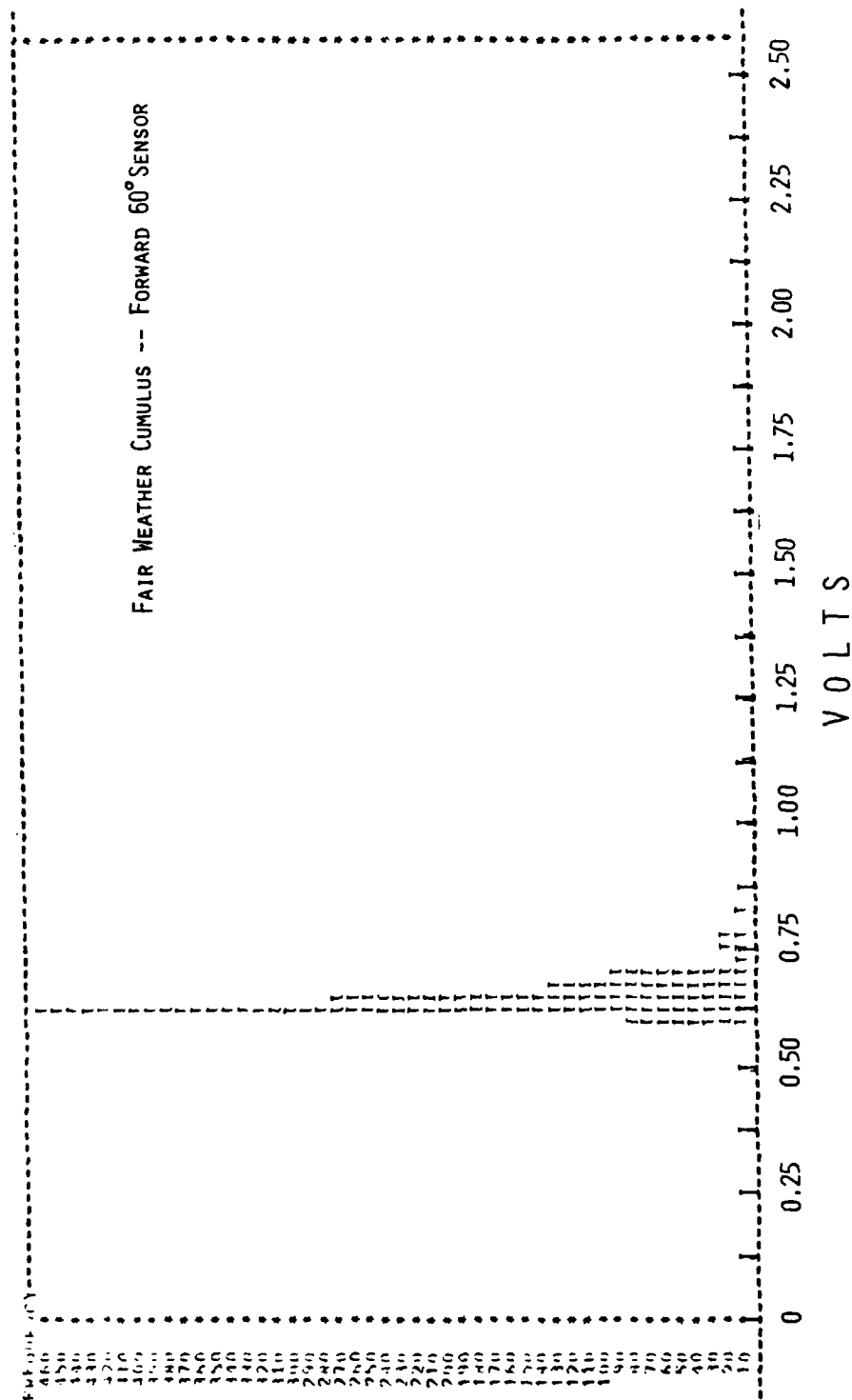
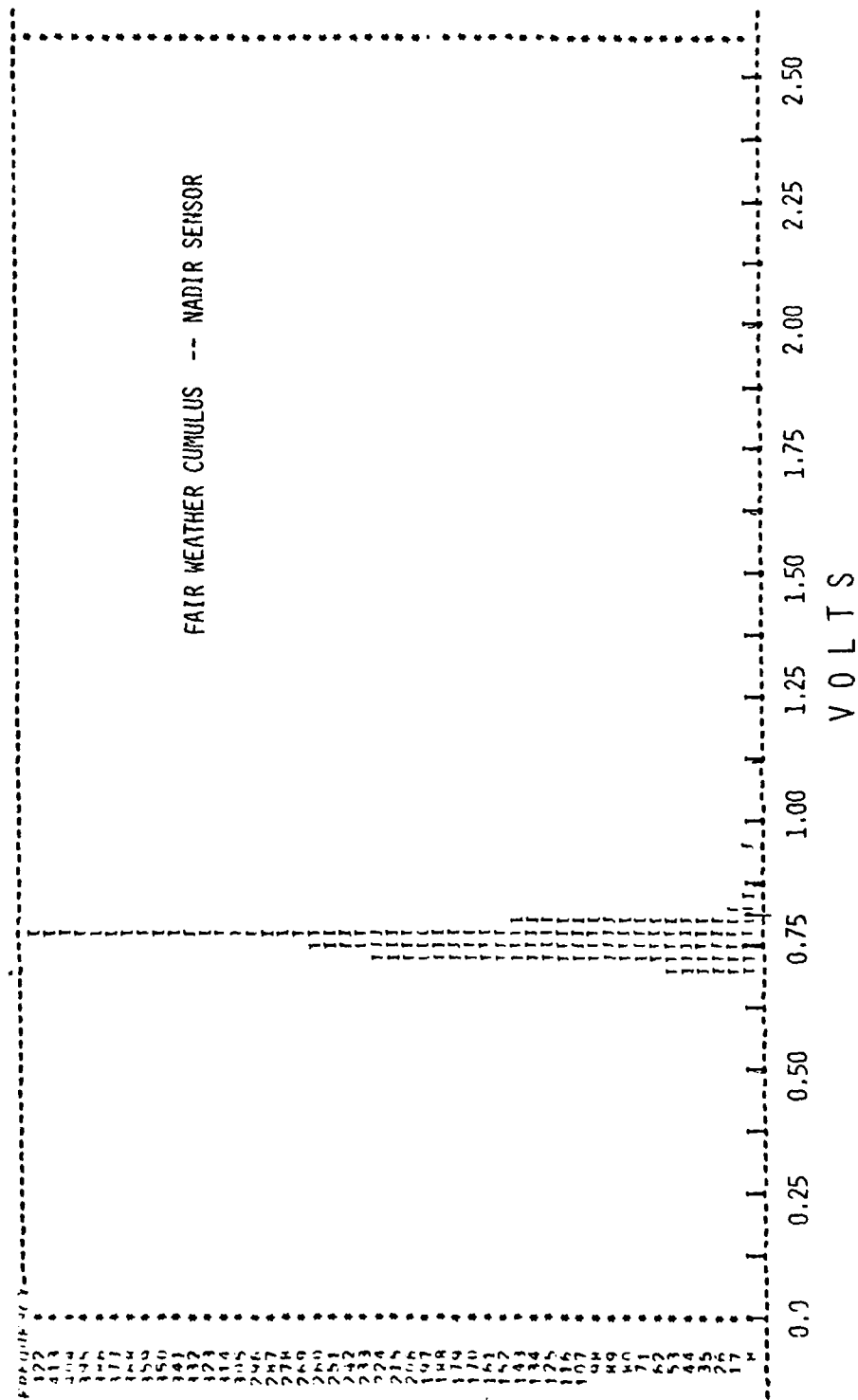Figure F 1. Frequency distribution – Fair Weather Cumulus -- Forward 60° sensor.

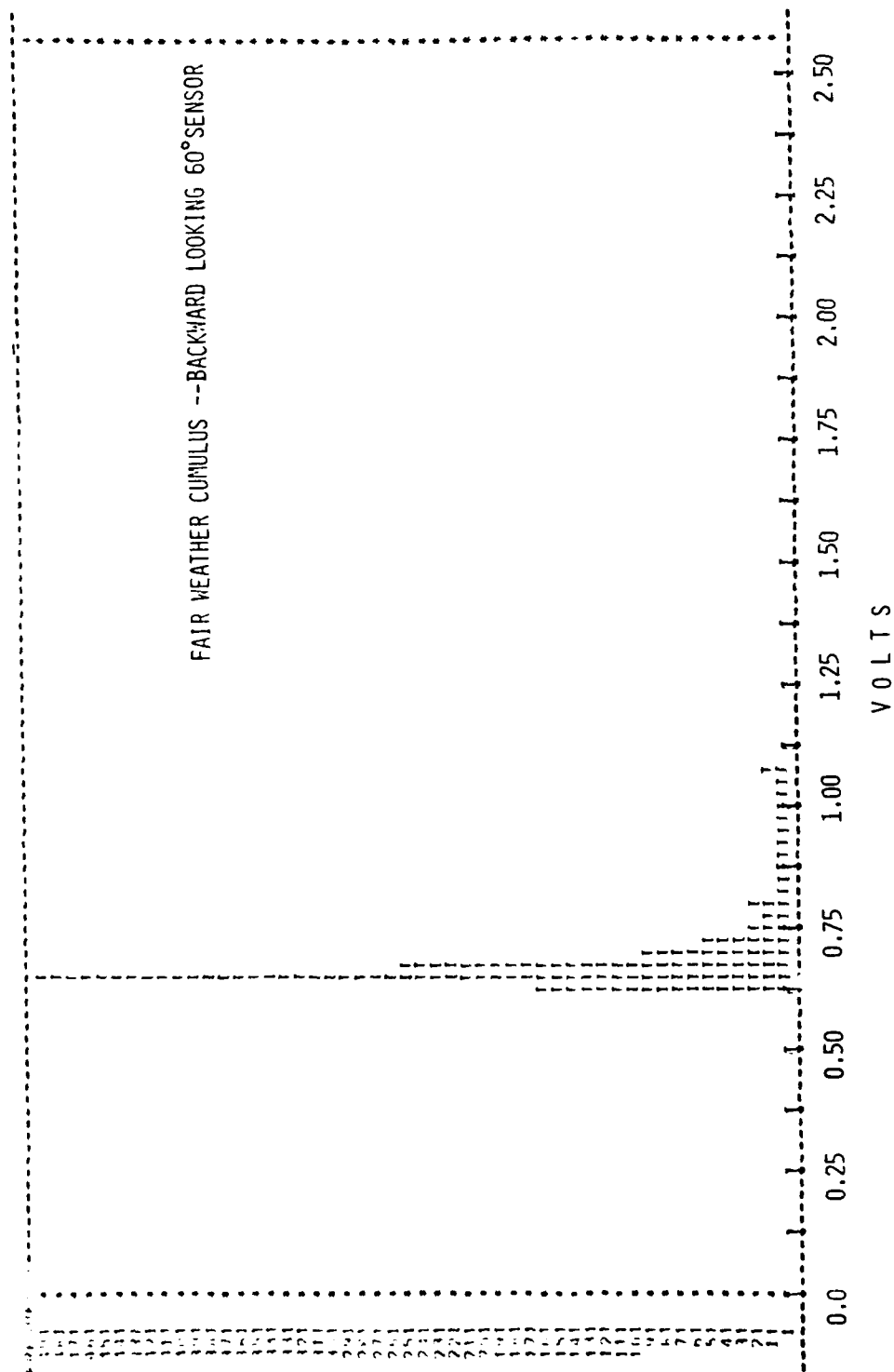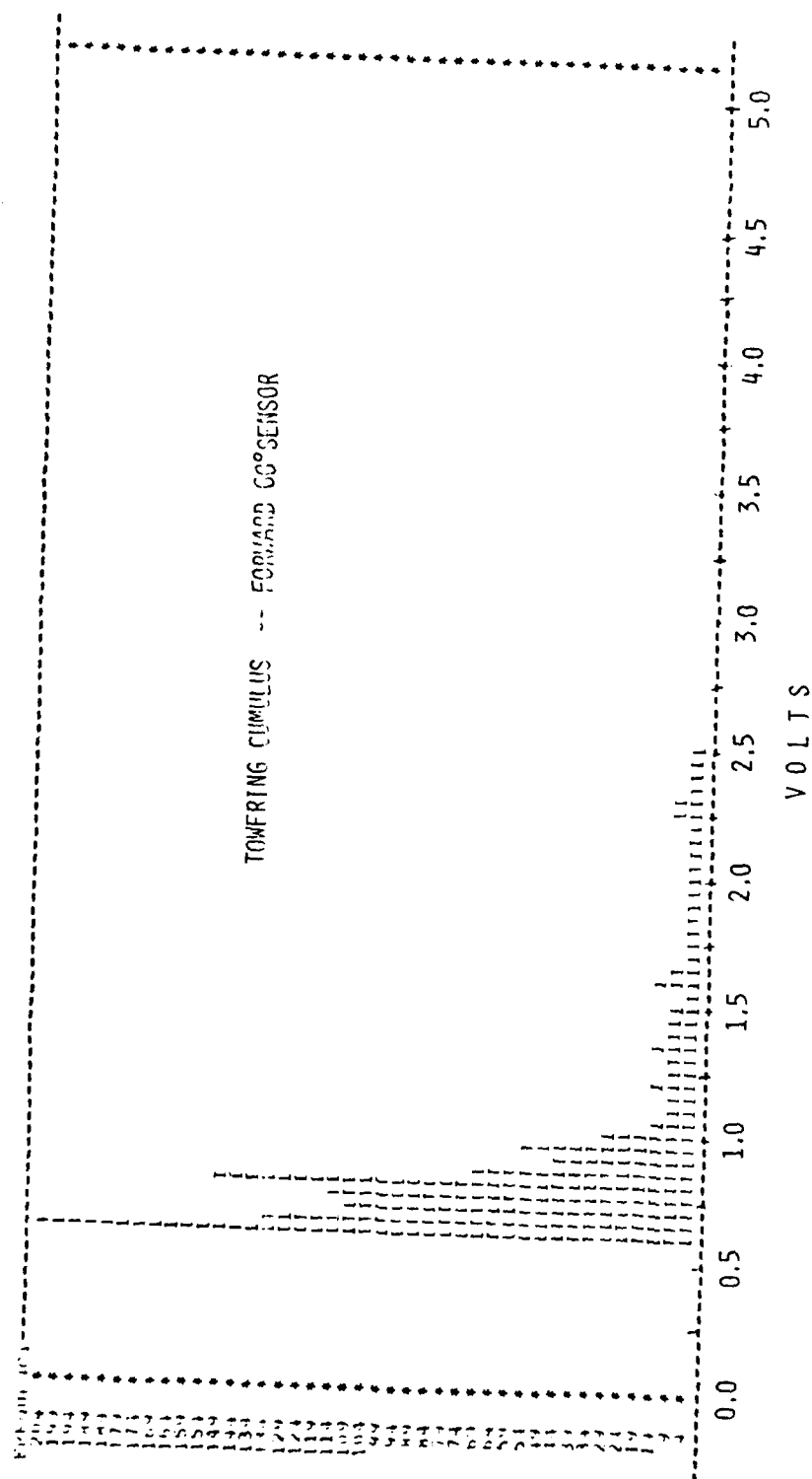Figure F 2. Frequency distribution – Fair Weather Cumulus -- Nadir Sensor

FAIR WEATHER CUMULUS --BACKWARD LOOKING 60°SENSOR

V O L T S

0.0   0.25   0.50   0.75   1.00   1.25   1.50   1.75   2.00   2.25   2.50

Figure F 3.   Frequency distribution – Fair Weather Cumulus -- Backward Looking 60° Sensor.

F-4

TOWERING CUMULUS -- FORWARD 60° SENSOR

VOLTS
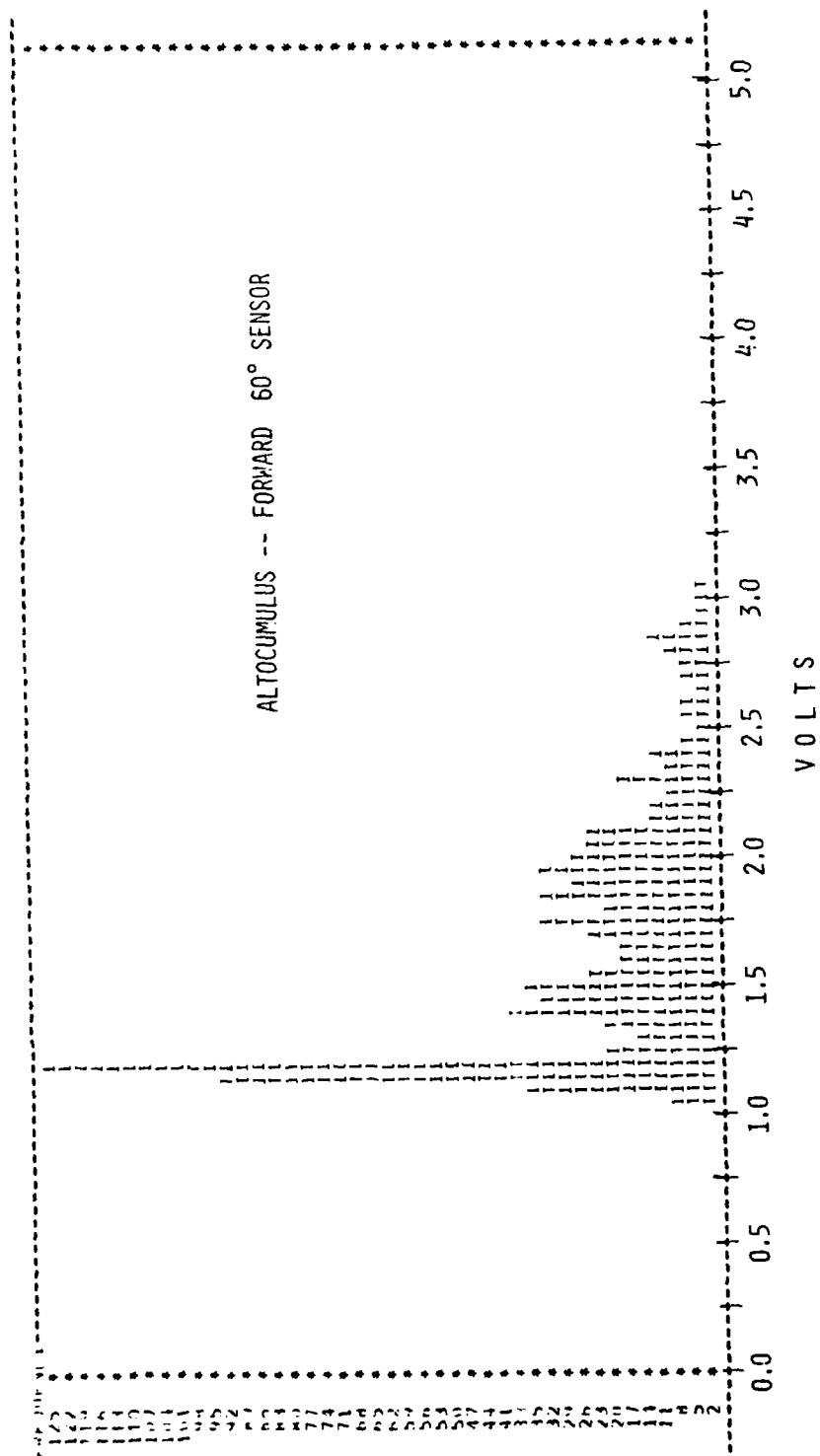
Figure F 4. Frequency distribution -- Towering Cumulus -- Forward 60° Sensor
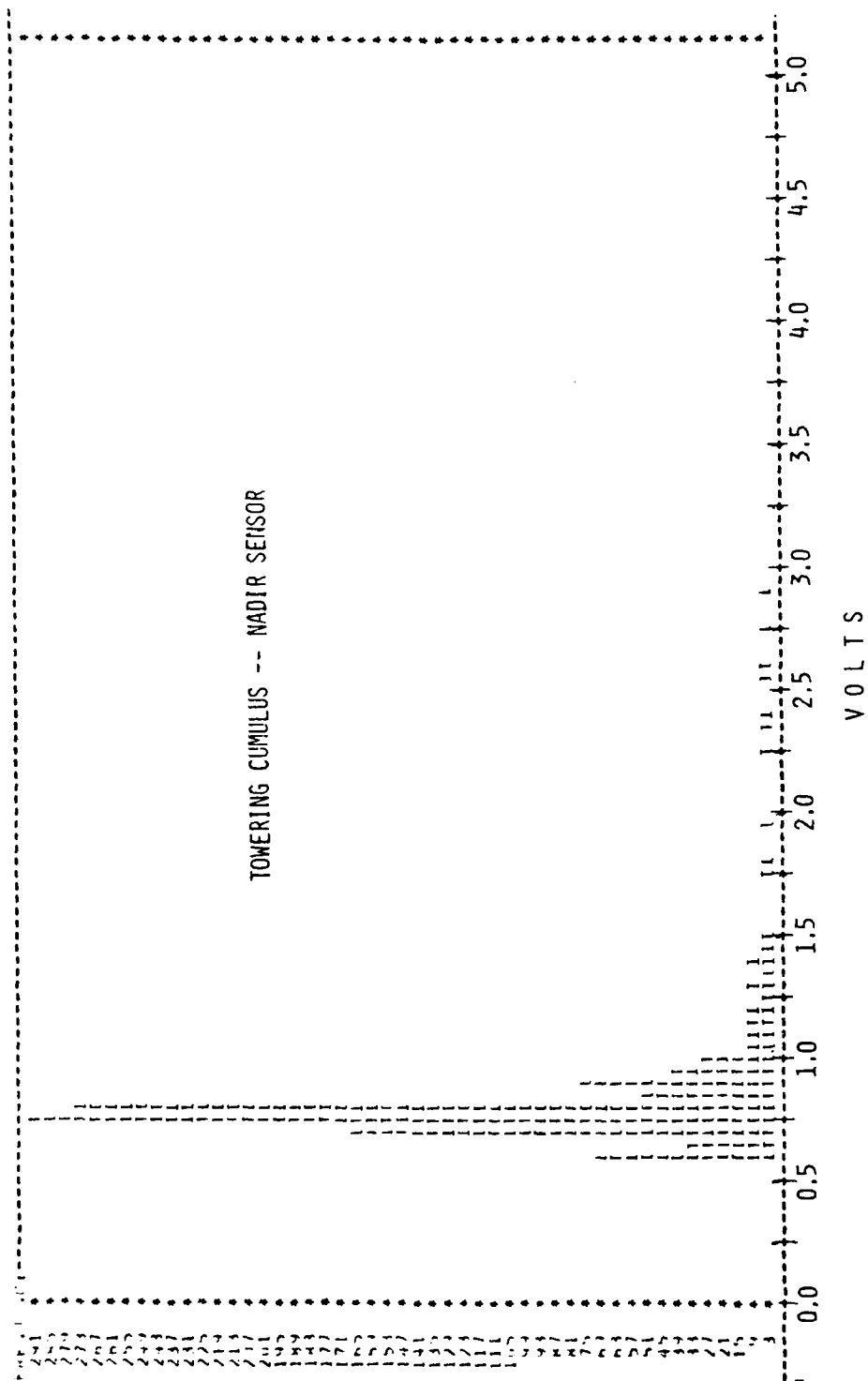
Figure F 5. Frequency distribution - Towering Cumulus -- Nadir Sensor

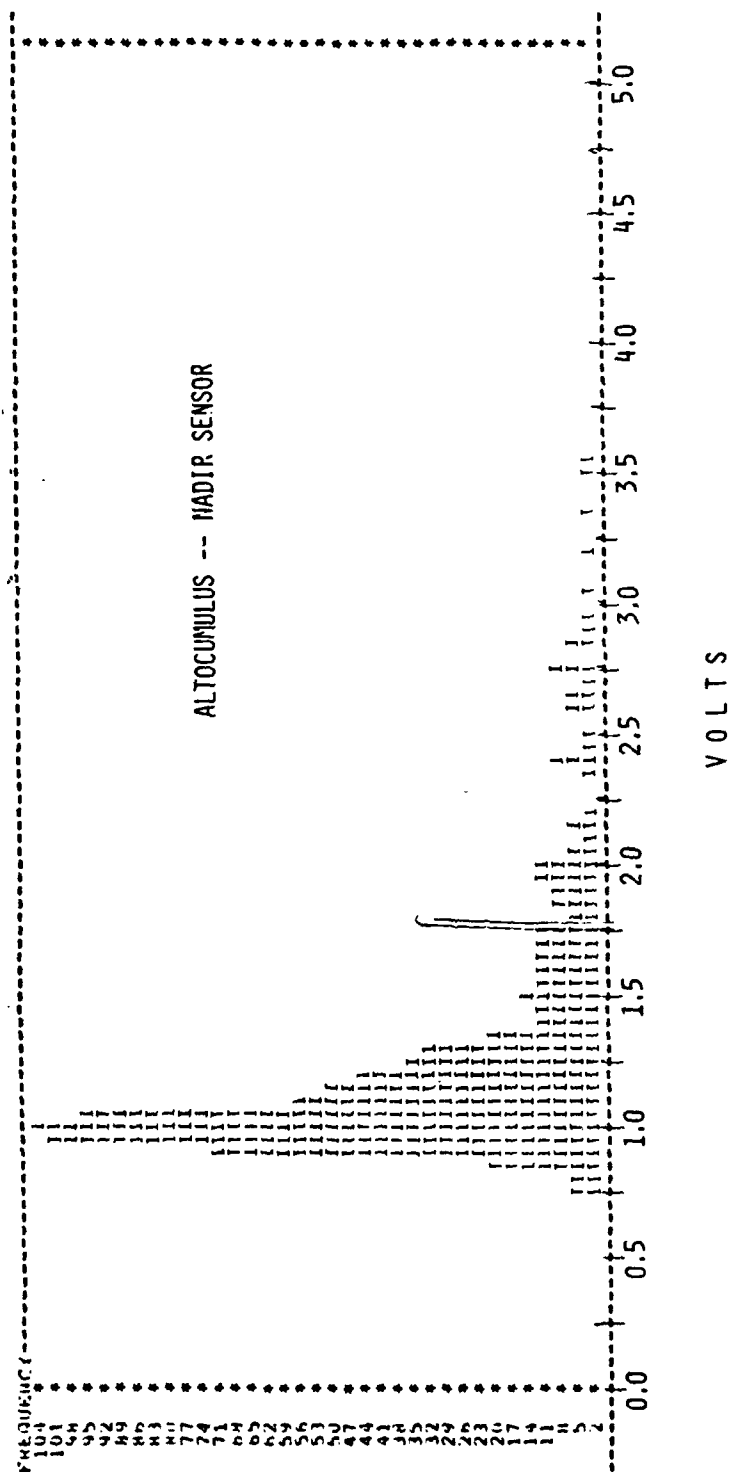TOWERING CUMULUS -- BACKWARD LOOKING 60° SENSOR

VOLTS

0.0   0.5   1.0   1.5   2.0   2.5   3.0   3.5   4.0   4.5   5.0
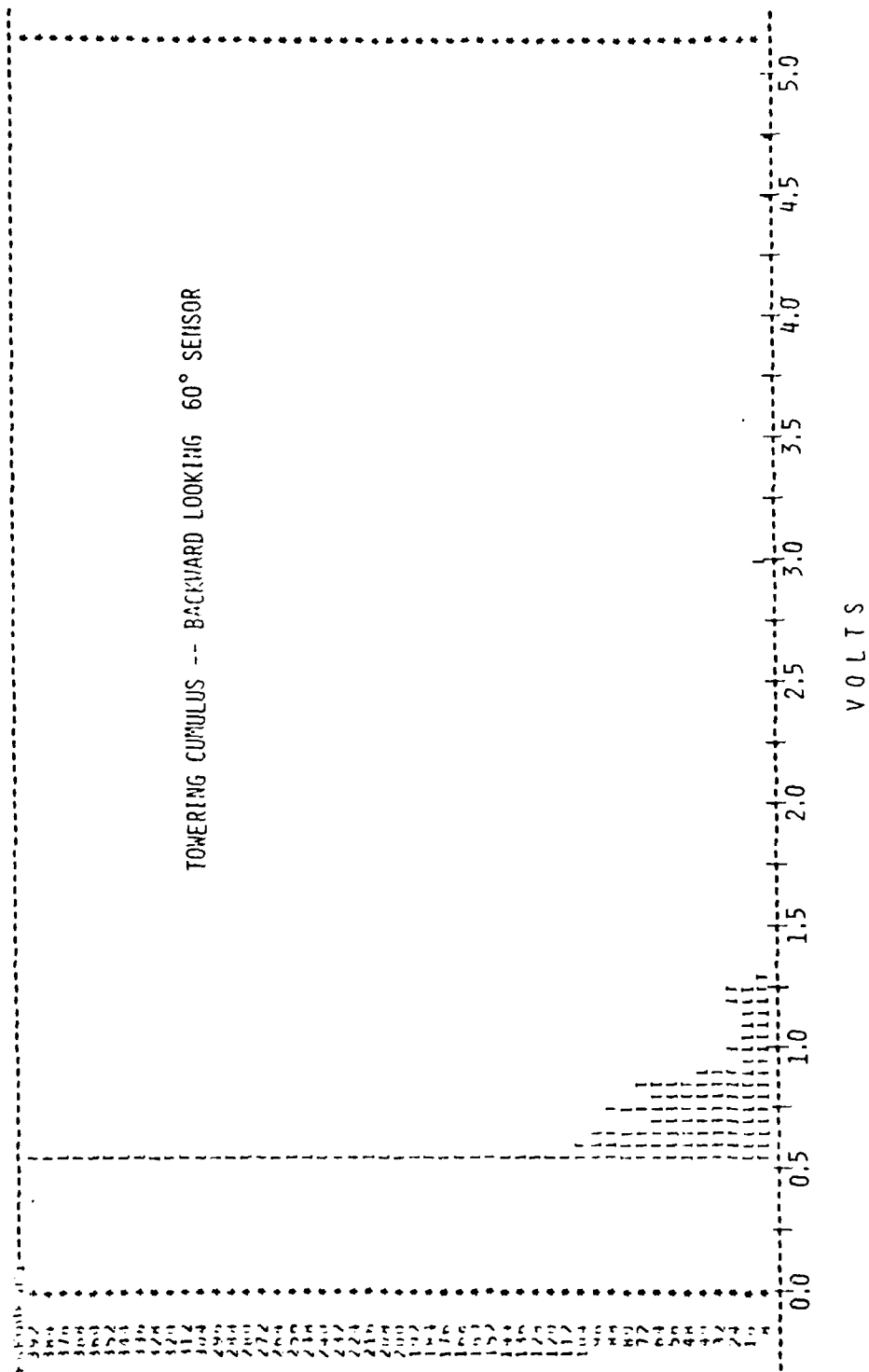
Figure F 6. Frequency distribution - Towering Cumulus -- Backward Looking 60° Sensor.

F-7

ALTOCUMULUS -- FORWARD 60° SENSOR

VOLTS

Figure F 7. Frequency distribution - Altocumulus -- Forward 60° Sensor.

F-8

ALTOCUMULUS -- NADIR SENSOR

V O L T S

Figure F 8.   Frequency distribution - Altocumulus -- Nadir Sensor

Figure F 9.   Frequency distribution - Altocumulus -- Backward Looking 60° Sensor.
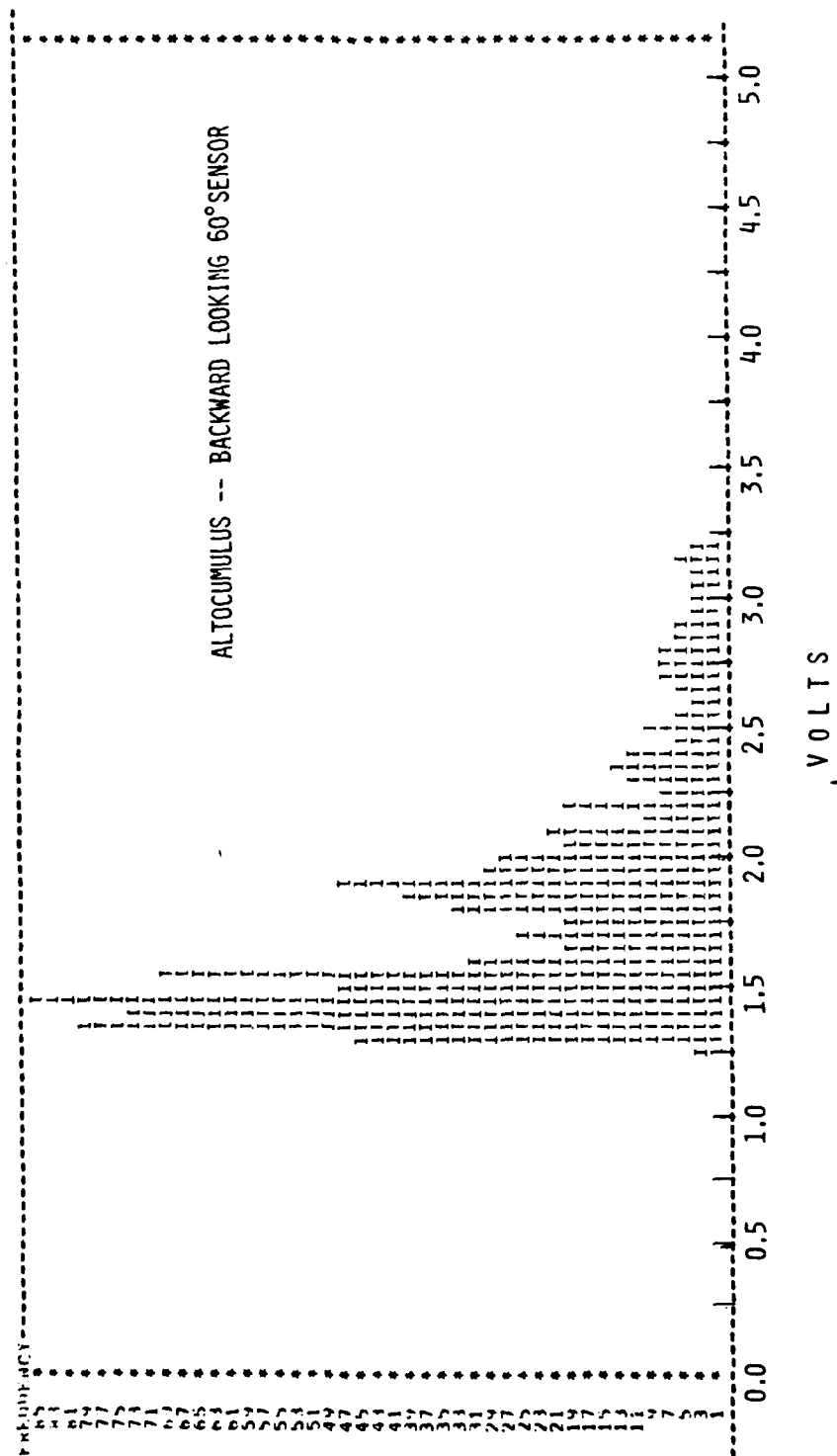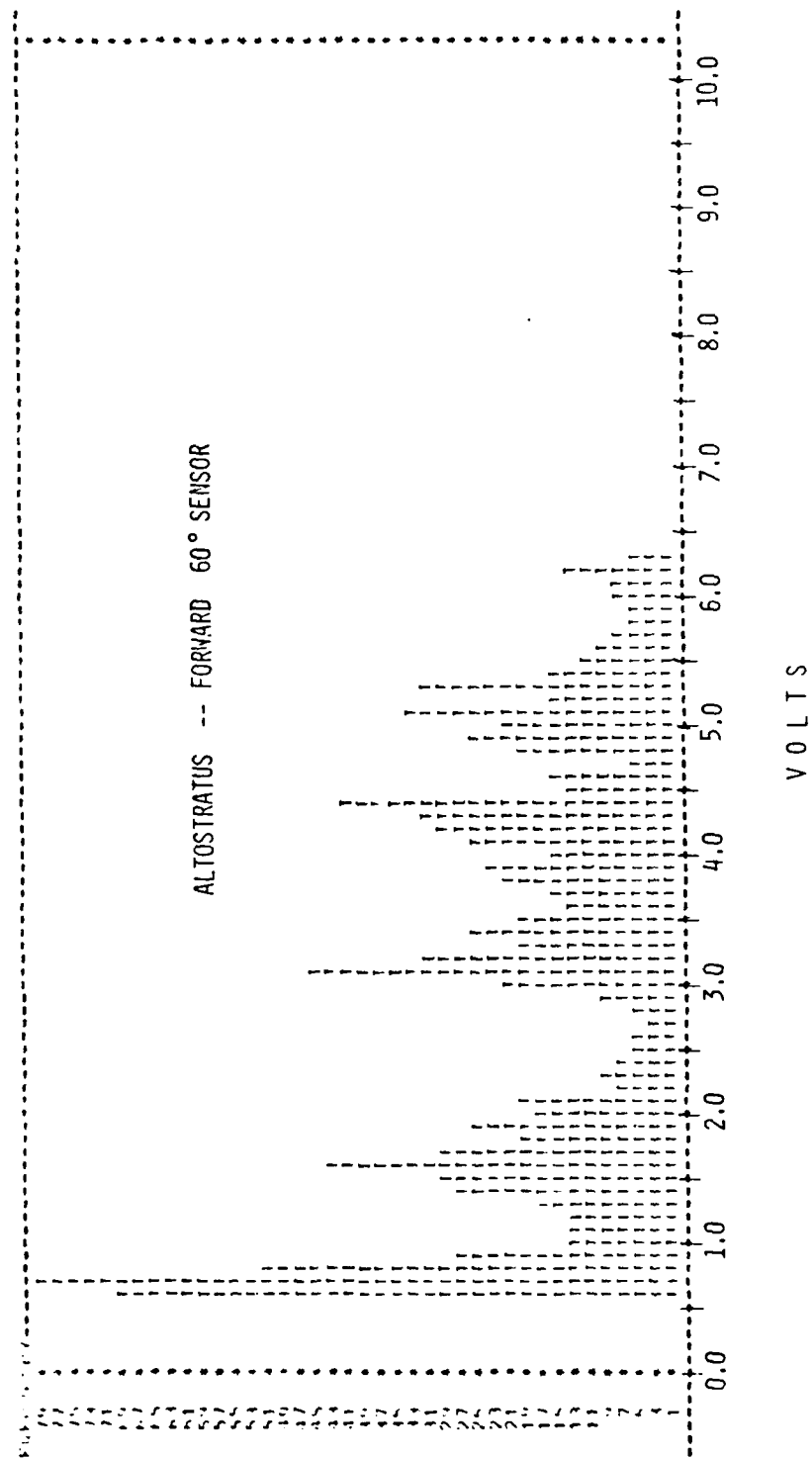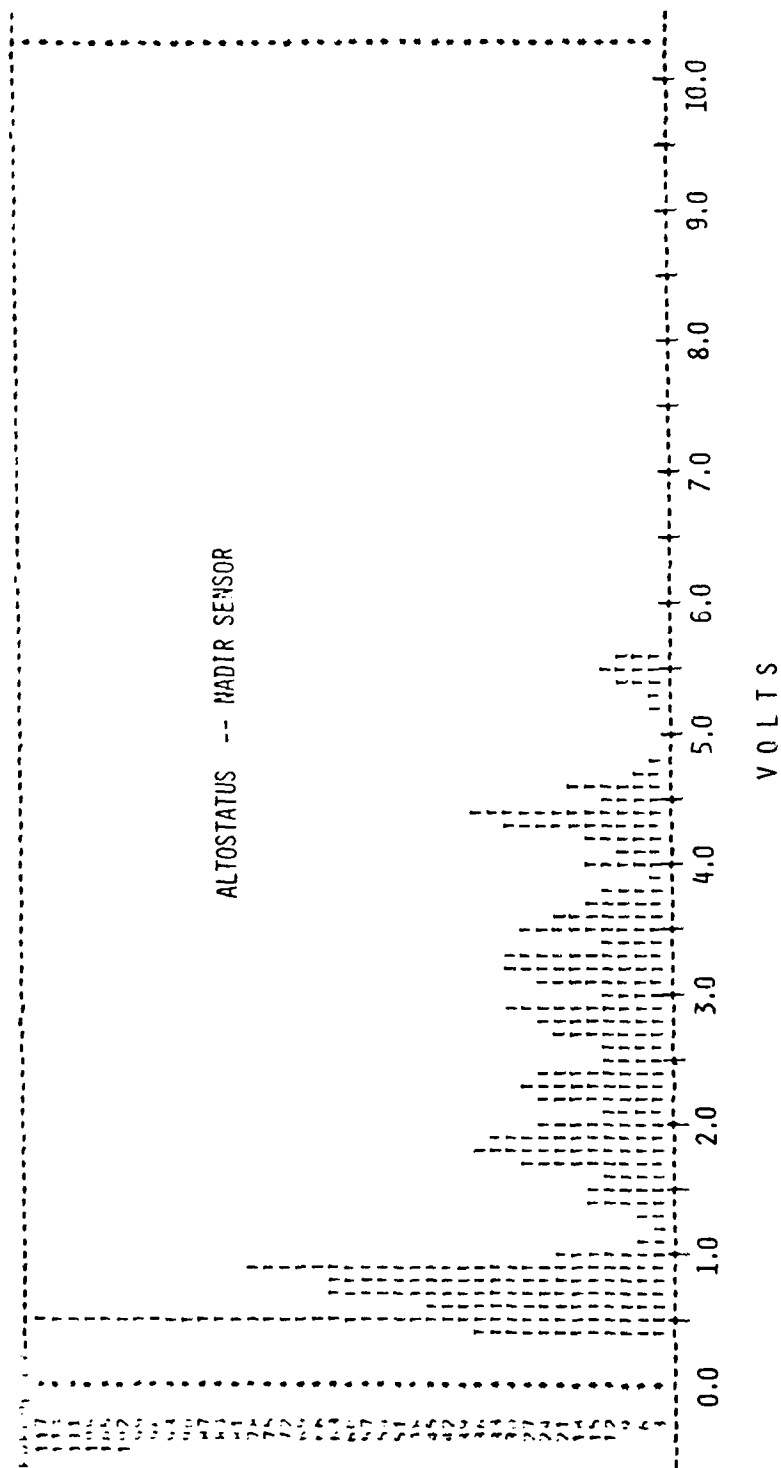
ALTOSTRATUS -- FORWARD 60° SENSOR

V O L T S

Figure F 10. Frequency distribution - Altostratus -- Forward 60° Sensor.

F-11

ALTOSTATUS -- NADIR SENSOR

V O L T S

Figure F 11. Frequency distribution - Altostratus -- Nadir Sensor

F-12

ALTOSTRATUS -- BACKWARD LOOKING 60°SENSOR

V O L T S

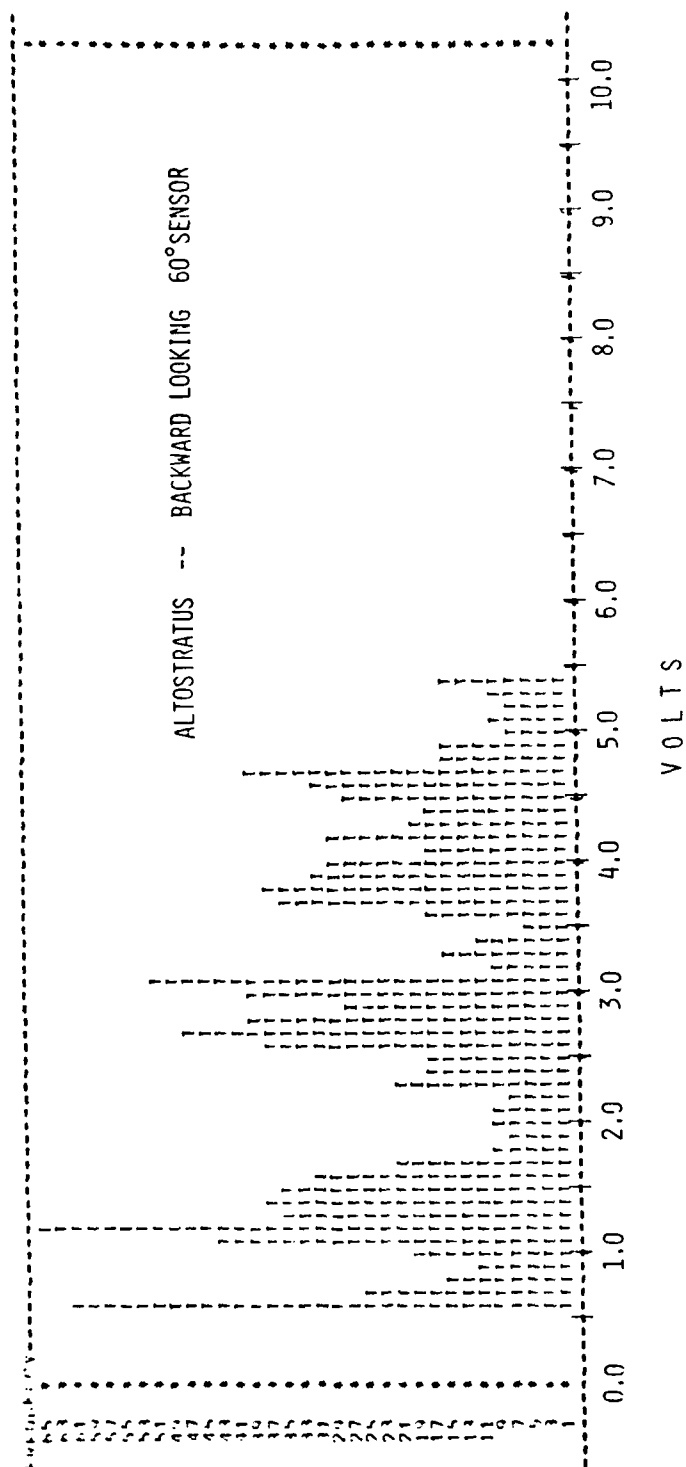0.0   1.0   2.0   3.0   4.0   5.0   6.0   7.0   8.0   9.0   10.0

Figure F 12. Frequency distribution - Altostratus -- Backward Looking 60° Sensor.